

MAPPING LYMAN CONTINUUM ESCAPE IN TOLOLO 1247–232

GENOVEVA MICHEVA^{1,2}, M. S. OEY¹, RYAN P. KEENAN^{1,3}, ANNE E. JASKOT^{4,5}, AND BETHAN L. JAMES⁶
(Accepted 19 September 2018)

¹University of Michigan, 311 West Hall, 1085 South University Ave, Ann Arbor, MI 48109-1107, USA

²Leibniz Institut für Astrophysik, An der Sternwarte 16, D-14482 Potsdam, Germany

³Steward Observatory, University of Arizona, 933 N. Cherry Ave, Tucson, AZ 85721, USA

⁴Department of Astronomy, University of Massachusetts, Amherst, MA 01003, USA

⁵Hubble Fellow

⁶Space Telescope Science Institute, 3700 San Martin Drive, Baltimore, MD 21218, USA

ABSTRACT

Low redshift, spatially resolved Lyman continuum (LyC) emitters allow us to clarify the processes for LyC escape from these starburst galaxies. We use *Hubble Space Telescope* (*HST*) WFC3 and ACS imaging of the confirmed low-redshift LyC emitter Tol 1247–232 to study the ionization structure of the gas and its relation to the ionizing star clusters. We perform ionization parameter mapping (IPM) using [O III] $\lambda\lambda$ 4959, 5007 and [O II] λ 3727 imaging as the high- and low-ionization tracers, revealing broad, large-scale, optically thin regions originating from the center, and reaching the outskirts of the galaxy, consistent with LyC escape. We carry out stellar population synthesis modeling of the 26 brightest clusters using our *HST* photometry. Combining these data with the nebular photometry, we find a global LyC escape fraction of $f_{\text{esc}} = 0.12$, with uncertainties also consistent with zero escape and with all measured f_{esc} values for this galaxy. Our analysis suggests that, similar to other candidate LyC emitters, a two-stage starburst has taken place in this galaxy, with a 12 Myr old, massive, central cluster likely having pre-cleared regions in and around the center, and the second generation of 2 – 4 Myr old clusters dominating the current ionization, including some escape from the galaxy.

Keywords: galaxies: evolution — galaxies: individual (Tol 1247–232) — galaxies: starburst — galaxies: star clusters: general — intergalactic medium — radiative transfer

1. INTRODUCTION

Escape of Lyman continuum (LyC) radiation from local star-forming galaxies (SFGs) has recently been detected from a handful of local galaxies at redshifts $0.02 \leq z \lesssim 0.33$ (Bergvall et al. 2006; Leitet et al. 2011, 2013; Leitherer et al. 2016; Borthakur et al. 2014; Izotov et al. 2016a,b; Chisholm et al. 2017; Izotov et al. 2018). The emitting galaxies comprise a sample of four blue compact galaxies (BCGs; e.g., Thuan & Martin 1981), one Lyman Break analog (LBAs; Heckman et al. 2005; Overzier et al. 2009), and six Green Peas (GPs; Cardamone et al. 2009). The confirmed low-redshift LyC emitting GPs (Izotov et al. 2016a,b, 2018) have escape fractions in the range 6-46%, but being at redshifts $z \sim 0.3$ they remain unresolved even in Hubble Space Telescope (*HST*) images. These spatially unresolved galaxies do not allow for a detailed investigation of the mechanisms behind the leakage of LyC.

The four LyC-emitting BCGs Haro 11, Tol 1247–232, Mrk 54, and Tol 0440–381 (Bergvall et al. 2006; Leitet et al. 2013; Leitherer et al. 2016; Chisholm et al. 2017), have lower escape fractions of a few percent, but are much closer, at $0.02 \leq z \leq 0.048$. At such redshifts, *HST* resolution is able to reveal the morphology and ionization structure of the interstellar medium (ISM)

and allows identification of the star-forming regions responsible for LyC escape. Hence, these galaxies offer the opportunity to clarify the processes behind the observed LyC leakage.

Tol 1247–232 is at a luminosity distance of 213 Mpc ($z = 0.048$) and hence allows for such a spatially resolved investigation into the morphology of the ionized gas and relation to super star clusters (SSCs). The escape fraction of Tol 1247–232 has been measured four times, with two different instruments, being consistently non-zero in all measurements (Leitet et al. 2013; Leitherer et al. 2016; Puschnig et al. 2017; Chisholm et al. 2017). This galaxy therefore offers a spatially resolved view of the ionization structure and morphology of a confirmed LyC emitter (LCE).

The technique of ionization parameter mapping (IPM) is well suited for such an investigation. IPM was first applied to H II regions in the Small (SMC) and Large Magellanic Clouds (LMC; Pellegrini et al. 2012), to identify optically thin H II regions and trace the escape of LyC photons from star-forming regions into the interstellar medium. Further applications of this technique have detected large-scale optically thin regions in NCG 5253 (Zastrow et al. 2011), NGC 3125 (Zastrow et al. 2013), and Haro 11 (Keenan et al. 2017), consistent with LyC

escape into the circumgalactic medium and beyond.

Of these three galaxies, Haro 11 is a confirmed LCE at $z = 0.02$ (Bergvall et al. 2006; Leitet et al. 2011). IPM analysis of this object (Keenan et al. 2017) reveals some surprising and important results. Whereas Knot C has been assumed to be the LyC source because of its strong Ly α emission, IPM indicates that this region is optically thick in the LyC, and instead, Knot A is strongly indicated as the source of the leakage. IPM also suggests that Knot B may be optically thin as well (Keenan et al. 2017), and it may host a low-luminosity active galactic nucleus (Prestwich et al. 2015), which is also conducive to escape of ionizing photons. It is therefore unclear which of the three bright knots in Haro 11 is responsible for the observed escape of LyC flux, and in particular, what the relationship is between LyC emission and Ly α emission.

In this paper, we explore the LyC radiative transfer in Tol 1247–232. Here, IPM paints a much clearer picture, easily revealing the dominant source of the ionizing radiation. In Section 2 we present the broad- and narrowband *HST* imaging data used in the analysis, describe the procedure of the continuum subtraction, and the IPM technique. Section 3 presents the stellar population analysis of all bright knots (“clusters”) inside the galaxy, and on the galaxy as a whole. We estimate the global LyC escape fraction in Section 4, discuss the implications of our analysis in Section 5, and present our conclusions in Section 6. The appendix provides a comparison between different methods for continuum subtraction in Section B, and supplementary data from the modeling of the spectral energy distribution of the clusters in Section C. Throughout this paper, we assume Λ CDM cosmology with $H_0 = 70 \text{ km s}^{-1} \text{ Mpc}^{-1}$, $\Omega_M = 0.3$, and $\Omega_\Lambda = 0.7$, and hence a luminosity distance to Tol 1247–232 of $D_L = 213.1 \text{ Mpc}$ at $z = 0.048$. All photometry is in the AB magnitude system.

2. NEBULAR ANALYSIS

We obtained *HST* WFC3 and ACS imaging in broadband and narrowband filters (P.I. Oey, PID 13702) that sample the *U* (F336W) and *V* bands (F547M) on the WFC3, and [O II] λ 3727 (FR388N) and [O III] λ 4959,5007 (FR505N) on the ACS. Additional WFC3 data (P.I. Östlin¹, PID 13027) exist for this galaxy in *B* (F438W), *R* (F775W), H α (F680N), H β (FQ508N), and far ultraviolet (FUV) F125LP and F140LP, which we used to complement the coverage of our target. The exposure times were 1208 s (F125LP and F140LP), 1030 s (F336W, P.I. Oey), 900 s (F336W, P.I. Östlin), 2710 s (FR338N), 732 s (F438W), 2355 s (FR505N), 1340 s (FQ508N), 1095 s (F547M), 740 s (F680N), and 600 s (F775W). We resampled all images to the larger pixel scale of the ACS of 0.05 arcsec. The filters are illustrated in Figure 1. Unless other-

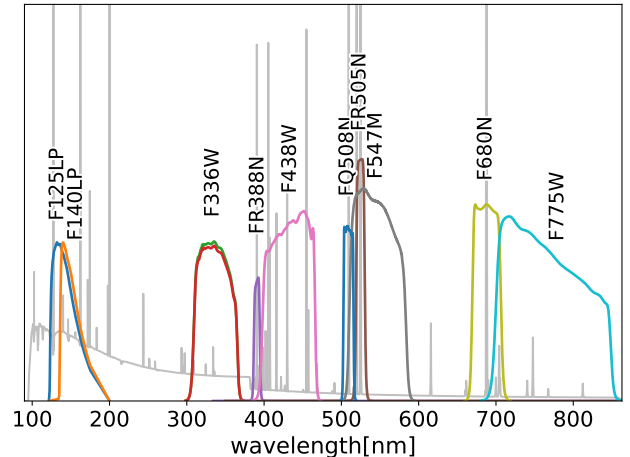


Figure 1. All *HST* filters utilized in this work, with an example galaxy SED at the redshift of Tol 1247–232, $z = 0.048$. Note that F336W and F438W bracket the Balmer break at this redshift.

wise stated, hereafter we will refer to [O II] λ 3727 and [O III] λ 4959,5007 as simply [O II] and [O III], respectively. We note that the F125LP filter contains the Ly α line, which cannot be modeled by standard population synthesis tools. The filter is broad, however, and is not dominated by line emission, so the line flux is not significant in our case.

To calibrate data, we used `pysynphot` with the observing mode given from the PHOTMODE header keyword, and assuming an infinite aperture. In practice, the aperture radius was set to 2 arcsec for the narrowband data, and 6 arcsec for the broadband data. All of our photometry therefore is measured relative to an infinite aperture zeropoint. To facilitate discussion of different galaxy regions, we introduce a naming convention, defined in Figure 2a.

2.1. Continuum subtraction

The four narrowband filters target the named [O II], H β , [O III], and H α lines. To isolate the line flux in each filter one must remove the contribution of the underlying continuum. We use F336W, F438W, F547M, and F775W, respectively, as off-line continuum filters, and estimate the line flux as $f_{\text{online}} - \mu f_{\text{offline}}$.

There are several methods for obtaining the scaling factor μ , producing either spatially resolved values (e.g., Hayes et al. 2009; James et al. 2016), or a single effective μ (e.g., Böker et al. 1999; Kennicutt et al. 2008; Hong et al. 2014; Keenan et al. 2017). The advantage of the former is that it accounts for spatial variations of the scaling factor, arising from its dependence on the color of the underlying stellar population, which varies from place to place. Figure 2a shows that there are indeed color gradients evident in Tol 1247–232, with the central Region A having blue colors hinting at a young population, and redder, older populations to the north in Region B and to the south-west in Bar I. Figure 2b

¹ Spelled Oestlin in the HST proposal archive

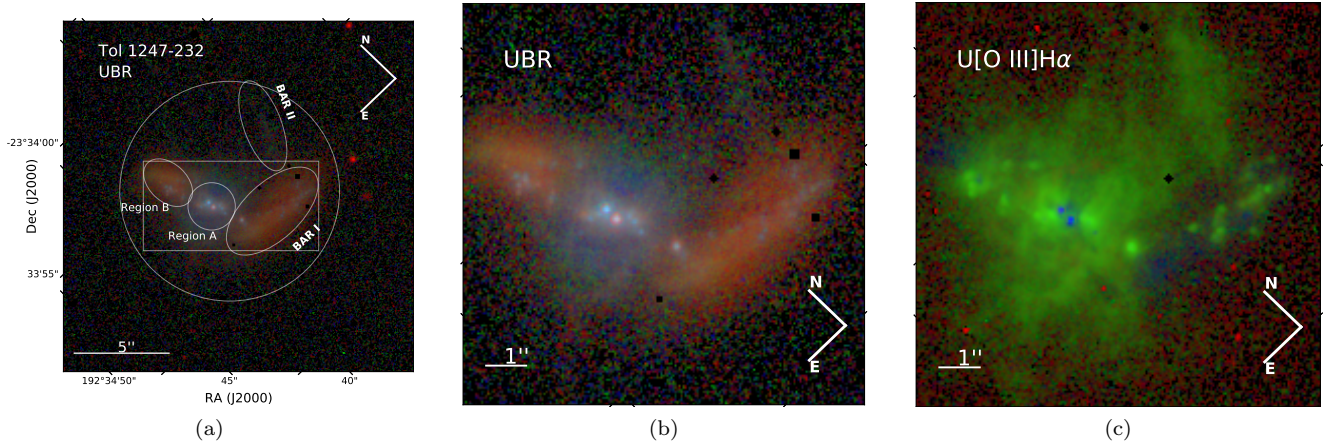


Figure 2. (a) A false color image of Tol 1247–232 with broadband F336W, F438W, and F775W as the blue, green, and red channels, respectively. The central Region A, coincident with the size and location of the *HST*/COS aperture in Puschnig et al. (2017), is indicated with a small white circle. Region B to the north of A is indicated by a white ellipse. Bar I and Bar II to the southwest and west of A, respectively, are also marked by ellipses. The white rectangle shows the area used to estimate the continuum scaling factor μ in Section 2.1. The large white circle indicates the aperture used for photometry on the total galaxy area. (b) Zoom of the galaxy region. Blue knots are visible not only in Region A, but also in B and Bar I. (c) Zoom of the galaxy with broadband F336W, and continuum-subtracted [O III], and H α images as the blue, green, and red channels, respectively. Bar II is clearly visible here, and appears to be emission line-dominated. At the distance of Tol 1247–232, 1 arcsec corresponds to 0.94 kpc.

is a zoom of the galaxy, showing smaller-scale variations in the stellar population. Puschnig et al. (2017) account for the presence of color gradients by using spatially resolved SED fitting to estimate continuum subtraction in their analysis of the distribution of Ly α emission in Tol 1247–232. However, this method is highly model-dependent, and determining the continuum scale factor is fraught with uncertainties, as we demonstrate in Section 3.2.

We therefore use the mode method of Keenan et al. (2017) to estimate a single scaling factor μ across the entire galaxy. This method is based on evaluating the mode of the pixel histogram of the continuum-subtracted image as a function of the scaling factor μ . For each of the four emission lines, the mode is computed over an area covering most of the galaxy, indicated by the white rectangle in Figure 2a. This area does not include Bar II. However, as can be seen from the superposition of Figures 2b and 2c, Bar II contains almost no visible stellar emission, being strongly dominated by nebular emission. Including Bar II would therefore only contribute background-dominated noise in determining the continuum scale factor, and we have therefore omitted Bar II from the region used to estimate μ . Further, we note that the scaling factor one obtains from the white rectangle in Figure 2a and from only Region A, agree to 90%.

Figure 3 shows the break in the mode versus μ function, indicating the location of the optimal μ for each filter. This break indicates the transition from under-subtraction to oversubtraction of the continuum (see Keenan et al. 2017). The observed breaks indicate $\mu = 0.52, 0.94, 0.80,$ and 0.84 for [O II], H β , [O III], and H α , respectively. Since the mode depends on the

bin size, we have explored all bin sizes from 0.1 to 20σ in steps of 0.1σ , where σ is the standard deviation of the pixel fluxes inside the white rectangle in Figure 2a. Beyond a certain bin size, the behavior of the mode as a function of μ converges to produce a break at the same position for all larger bin sizes. In the figure we show the mode function for different bin sizes, starting from the smallest bin beyond which all bin sizes produce a break at the same μ . We also show a few larger bins to demonstrate the robustness of that convergence. The on-line and off-line fluxes are corrected for Galactic extinction using the Schlafly & Finkbeiner (2011) reddening curve before the subtraction. Due to line contamination in the F547M continuum filter, our [O III]/[O II] ratios are lower limits, as discussed in Appendix A.

In Appendix B, we compare the mode method to other methods for determining the global scale factor. The agreement between the methods is good, and we conclude that the mode method is a relatively straightforward and efficient way to obtain the scaling factors. One clear advantage over other methods is that the break in the mode function, and hence the value of μ , is unambiguous and easy to identify. In what follows, we use the continuum-subtracted images produced with the mode method.

2.2. Ionization parameter mapping

The technique of ionization parameter mapping (IPM) spatially explores the ionization structure of the interstellar medium (e.g., Pellegrini et al. 2012; Zastrow et al. 2011, 2013; Keenan et al. 2017). Regions with high ionization can be traced via, e.g., O $^{+2}$ or S $^{+2}$ emission, which require photons with energies significantly higher than what is needed to ionize hydrogen. The detection

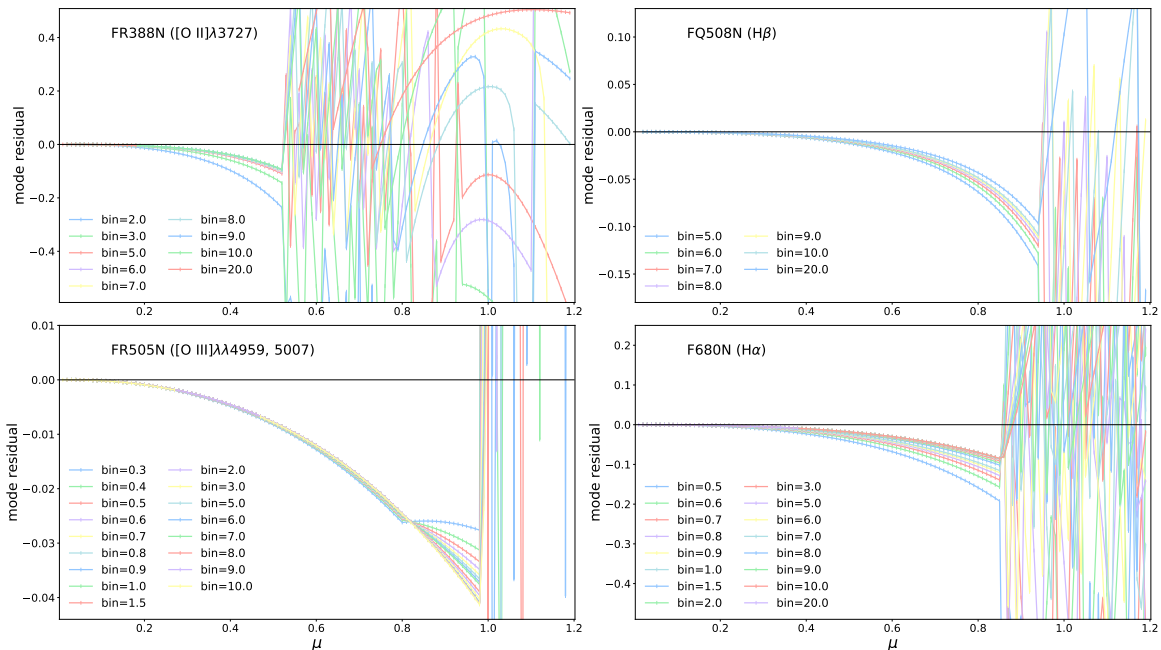


Figure 3. Mode method for continuum subtraction (Keenan et al. 2017): Scaling factor μ as a function of the mode. For convenience, on the y -axis, we plot the residual between the mode and a linear fit to the first few mode points. This presentation better highlights the breaks at optimal μ . For all displayed bin sizes, the mode function shows a strong break at about the same μ value. In each panel this break represents the optimal scaling factors, which are 0.52, 0.94, 0.80, and 0.84 for [O II], H β , [O III], and H α , respectively.

of lines from these species therefore indicates that hydrogen is predominantly ionized in such regions. Further away from the source of ionizing photons, the ionization state of hydrogen ordinarily transitions to neutral, for optically thick conditions. In this transition region, low-ionization species dominate and can be traced via, e.g., O $^+$ or S $^+$ lines. While other species can be used as tracers, a practical constraint is that the emission lines be strong enough to be easily detected.

We use our continuum-subtracted [O III] and [O II] imaging to serve as the high and low ionization tracers, respectively. The [O III]/[O II] ratio, often strong in young starbursting regions, is a good proxy of the ionization parameter U (e.g., Jaskot & Oey 2013). Figure 4a shows the [O III]/[O II] ratio. As discussed in Appendix A, the [O III]/[O II] values are lower limits, due to the over-subtraction of the continuum in the FR505N filter. High values of this ratio (coded blue) are indicated throughout the central region of the galaxy, including along the minor axis both to the east and west of the center, clearly reaching the outskirts of the galaxy. These ionized regions are broad, extending ~ 3 kpc from the center of Region A in both directions. Region A itself appears completely ionized, and has a diameter of 2.5 arcsec (2.3 kpc), corresponding to the size of the COS aperture. In Region B and Bar I, areas with [O III]/[O II] ≤ 1 are visible (coded red in Figure 4a), indicating that they are dominated by low-ionization gas. In particular, Bar I appears to have low [O III]/[O II], although some islands of higher ionization are clearly visible. This is consistent with its reddish appearance

in the *UBR* composite in Figure 2b, suggesting that Bar I consists of an older stellar population. In contrast, Bar II, which is dominated by nebular emission in Figures 2b and 2c, shows on average high [O III]/[O II] ratios. As mentioned in Section 2.1, this region requires external sources of ionization, since there are no obvious internal sources that could provide for the observed high [O III]/[O II] ratio. We further note that two circular regions in the north and south along the major axis, corresponding to the blue knots in Region B and Bar I, show high values of [O III]/[O II], but are almost completely surrounded by low-ionization zones, and are therefore likely optically thick. Only the large, circular, ionized central area appears to fully ionize the ISM to circumgalactic radii, implying that it is the origin of the ionizing photons responsible for the observed LyC escape. This region corresponds to the very blue central Region A of the *UBR* composite image in Figure 2, and is approximately indicated by the white circle in Figure 2a. As seen in Figure 4a, it appears to be even larger when examined via IPM.

Figures 4b and 4c show high [O III]/H α and simultaneously low [O II]/H α , spatially coincident with the optically thin areas and the central galaxy region, confirming our interpretation of the IPM in Figure 4a. Figure 4b in particular shows [O III] emission dominant over H α throughout most of the galaxy area. This is also visible in the three-color image in Figure 2c, which is completely dominated by emission in the green channel, i.e., in [O III]. Only the two central knots appear free of both [O III] and H α emission in this figure, which has

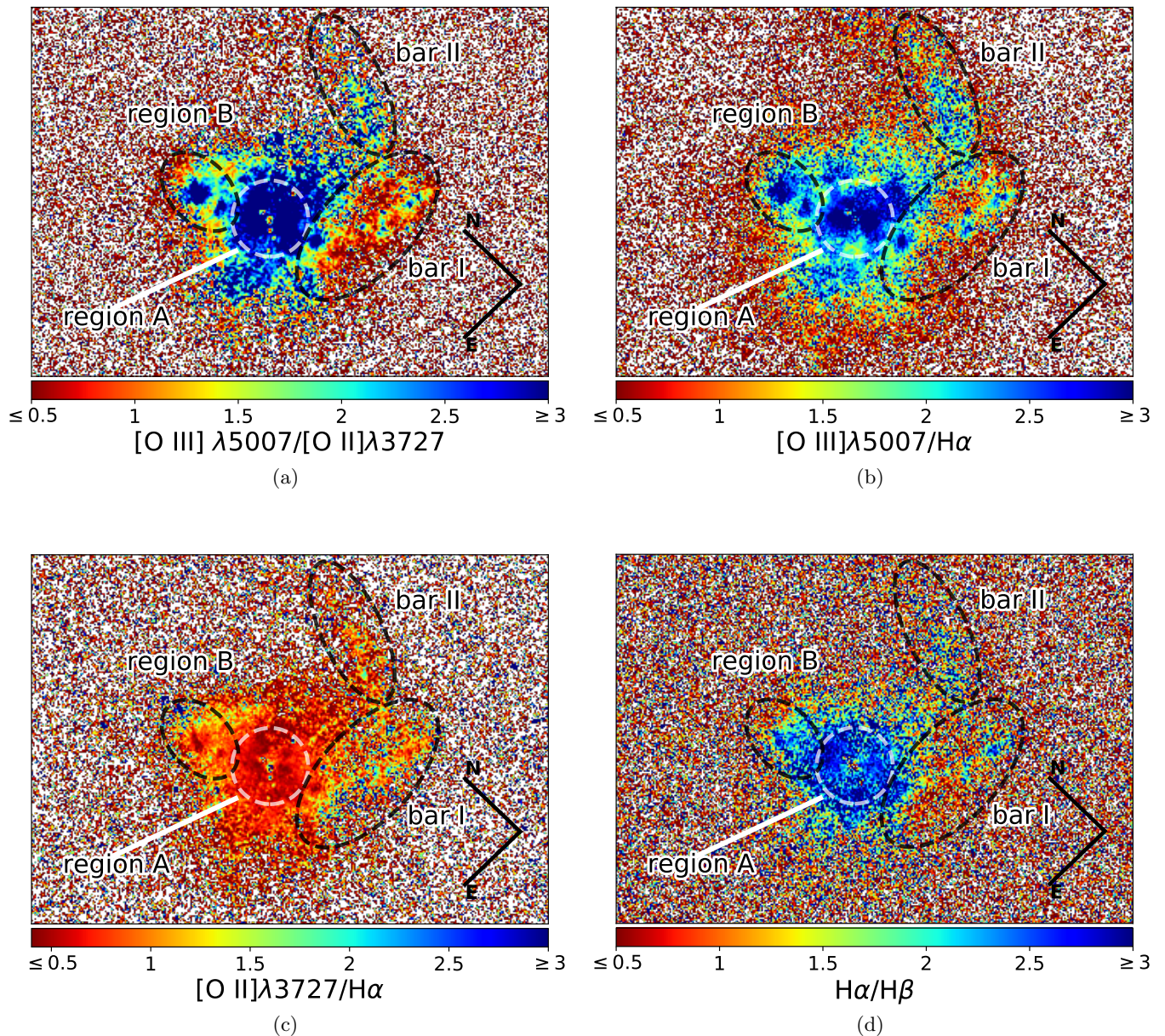


Figure 4. Ionization parameter mapping. Boundaries of Regions A (white dashed circle), B, Bar I and Bar II (black dashed ellipses), defined in Figure 2a, are overplotted for orientation. Panels (a), (b), (c) and (d) show the ratios of $[\text{O III}]/[\text{O II}]$, $[\text{O III}]/\text{H}\alpha$, $[\text{O II}]/\text{H}\alpha$, and $\text{H}\alpha/\text{H}\beta$ respectively. All ratios are based on continuum-subtracted images as described in Section 2.1. Region A has a diameter of 2.5 arcsec, corresponding to 2.3 kpc.

important implications for their interpretation as optically thin regions (see Section 4).

As already shown in Puschig et al. (2017), the average dust extinction in Region A is low. The $\text{H}\alpha/\text{H}\beta$ ratio map in Figure 4d shows that the dust extinction outside of Region A is also low. The observed high $[\text{O III}]/[\text{O II}]$ and low $[\text{O II}]/\text{H}\alpha$ values are therefore not due to high internal extinction.

3. STELLAR POPULATION

In the context of mapping the galaxy’s ionization structure, it is of interest to determine the nature of

the sources responsible for the observed ionization. We therefore examine the stellar populations that dominate our regions defined in Figure 2a. Figure 5 shows a zoom of the three major areas: Regions A, B, and Bar I. As mentioned earlier, Bar II has no detectable stellar population and is therefore omitted from this analysis. Several bright compact knots, labeled with numbers, are seen in the Figure. At the luminosity distance to Tol 1247–232 of 213 Mpc, our resolution of 0.05 arcsec corresponds to 47 pc per pixel. This is much larger than the typical sizes for open and globular clusters ($\lesssim 10$

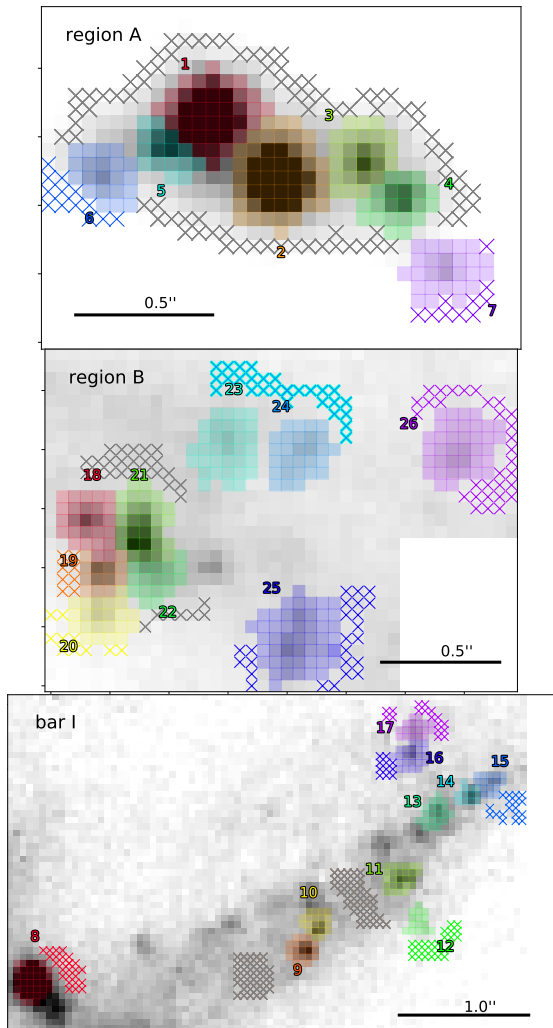


Figure 5. FUV continuum (F140LP) images of regions A, B, and Bar I, showing cluster IDs. The colors represent the pixel apertures, with corresponding cluster IDs shown in the same color. Colored crosses show sky regions for apertures marked in the same color, and gray crosses mark the sky regions common to all clusters without an individual sky region. Clusters 23 and 24 share a sky region.

pc), and we therefore cannot separate individual star clusters, unless they happen to be well isolated. Nevertheless, the spectral energy distribution (SED) of a knot consisting of several clusters will likely be dominated by the youngest, brightest population. For the remainder of this paper, we therefore refer to these knots as “clusters” and treat them as a single stellar population.

3.1. Cluster photometry

For cluster selection criteria, we require at least a 1σ detection in all four optical broadband filters, and in the

H α filter. We discarded objects that showed only noise in the FUV, i.e., older clusters were eliminated since they have negligible contributions to the ionization structure of the gas. To assess the contribution of the resulting 26 clusters in Figure 5 to the ionization budget of the galaxy, we first obtained their luminosity in each filter via pixel photometry. We manually selected pixels belonging to each cluster (color-coded squares in Figure 5), and then applied a background cutoff to remove pixels below the selected background level. The background regions are marked in Figure 5 as crosses. Clusters 1 through 5 in Region A all seem to be on the same background, marked by gray crosses, while clusters 6 and 7 in the same region are offset from the center, and are therefore assigned a different background region each, marked by crosses of the same color as their pixel aperture. Similarly, in Region B and Bar I, for all clusters which seemingly share the same background, the gray crosses mark the location of the selected background region, while for clusters that are either isolated or too offset from the main background area, we use separate regions, marked with crosses color-coded by the corresponding pixel aperture. The median background value of each of these regions is our estimate for the background flux in each pixel of the associated cluster apertures. The uncertainties on the photometry were calculated with the same formula used by the IRAF² PHOT task, using the standard deviation of the sky regions ($stdev$), the flux inside the apertures, and the area of both object ($area$) and sky apertures (N_{sky}), namely $err = \sqrt{flux/gain + area \times stdev^2 + area^2 \times stdev^2 / N_{sky}}$. The SED-fitting routine requires symmetric errorbars in the input photometry, and we therefore symmetrically propagate the flux error to magnitudes ($merr$) via $merr = 1.0857 \times err/flux$, even though for large uncertainties $\gtrsim 30\%$ the departure from symmetry is significant. For example, a symmetric magnitude error of 0.8 mag corresponds to a relative error of 0.74, and hence to non-symmetric magnitude errors of $^{+1.44}_{-0.60}$ mag. Table 1 summarizes the photometry for all 26 clusters in the available filters. Although in the SED fits we use photometry from our own F336W observations and from the repeated F336W observations with UVIS2 (PID 13027), we have omitted explicitly showing the latter in the table, because within the error bars it is fully consistent with our F336W data. The UVIS2 F336W photometry was included as a separate observation in the list provided to the SED-fitting routine.

² IRAF is distributed by the National Optical Astronomy Observatories, which are operated by the Association of Universi-

ties for Research in Astronomy, Inc., under cooperative agreement with the National Science Foundation.

Table 1. Photometry in magnitudes for clusters in Region A, Bar I, and Region B.

ID	N_{ap}	N_{sky}	F125LP (mag)	F140LP (mag)	F336W (mag)	FR388N (mag)	F438W (mag)	FQ508N (mag)	FR505N (mag)	F547M (mag)	F680N (mag)	F775W (mag)
Region A												
1	38	82	16.9 ± 0.1	16.7 ± 0.1	17.4 ± 0.1	17.7 ± 0.1	17.7 ± 0.1	17.7 ± 0.1	17.1 ± 0.1	17.6 ± 0.1	17.7 ± 0.1	18.0 ± 0.1
2	48	82	17.2 ± 0.1	16.9 ± 0.1	17.6 ± 0.1	17.9 ± 0.1	17.7 ± 0.1	17.7 ± 0.1	17.4 ± 0.1	17.5 ± 0.1	17.7 ± 0.1	17.6 ± 0.1
3	25	82	19.5 ± 0.2	19.3 ± 0.2	19.9 ± 0.1	19.6 ± 0.3	20.1 ± 0.1	19.6 ± 0.2	17.7 ± 0.1	19.0 ± 0.1	19.0 ± 0.1	20.2 ± 0.1
4	21	82	20.2 ± 0.2	19.9 ± 0.3	20.2 ± 0.1	19.9 ± 0.4	20.4 ± 0.1	19.8 ± 0.2	17.7 ± 0.1	19.1 ± 0.1	19.1 ± 0.1	20.6 ± 0.1
5	16	82	19.5 ± 0.2	19.2 ± 0.2	19.8 ± 0.1	19.7 ± 0.3	20.0 ± 0.1	19.5 ± 0.2	17.4 ± 0.1	18.8 ± 0.1	18.9 ± 0.1	20.2 ± 0.1
6	21	15	20.2 ± 0.2	20.0 ± 0.3	20.8 ± 0.2	20.1 ± 0.4	20.7 ± 0.2	20.1 ± 0.3	18.1 ± 0.1	19.5 ± 0.1	19.4 ± 0.1	20.8 ± 0.2
7	26	16	21.0 ± 0.3	20.6 ± 0.4	21.3 ± 0.2	21.2 ± 0.6	21.5 ± 0.2	21.3 ± 0.5	19.7 ± 0.2	20.8 ± 0.2	20.9 ± 0.3	21.7 ± 0.2
Error [%]	Region A		16.6	19.0	10.8	30.0	10.5	21.1	10.2	7.6	11.7	11.5
Bar I												
8	37	26	21.0 ± 0.3	20.5 ± 0.3	20.3 ± 0.1	19.7 ± 0.3	20.4 ± 0.1	19.7 ± 0.2	17.6 ± 0.1	19.0 ± 0.1	18.9 ± 0.1	20.3 ± 0.1
9	21	81	23.0 ± 0.9	(22.8)	23.1 ± 0.5	22.2 ± 1.0	23.4 ± 0.5	23.0 ± 1.0	21.1 ± 0.4	22.5 ± 0.4	22.2 ± 0.5	23.7 ± 0.6
10	20	81	23.4 ± 1.0	22.8 ± 1.0	23.3 ± 0.5	22.2 ± 1.0	23.5 ± 0.5	22.8 ± 1.0	20.9 ± 0.4	22.3 ± 0.3	22.0 ± 0.4	23.5 ± 0.6
11	26	13	23.0 ± 0.8	22.5 ± 0.9	22.9 ± 0.4	(23.0)	22.8 ± 0.4	22.6 ± 0.9	22.2 ± 0.7	22.5 ± 0.4	22.3 ± 0.5	22.4 ± 0.3
12	15	25	(24.4)	(23.6)	24.5 ± 0.9	(23.8)	24.4 ± 0.9	(23.8)	22.7 ± 0.9	23.6 ± 0.6	23.3 ± 0.8	24.0 ± 0.7
13	22	81	(23.9)	(23.2)	23.2 ± 0.5	22.0 ± 0.9	23.6 ± 0.6	22.8 ± 0.9	20.7 ± 0.4	22.3 ± 0.3	21.8 ± 0.4	24.2 ± 0.8
14	14	23	(23.9)	(23.2)	23.6 ± 0.7	(22.8)	23.5 ± 0.6	22.9 ± 1.0	21.0 ± 0.4	22.4 ± 0.4	22.3 ± 0.5	23.4 ± 0.6
15	16	18	(24.0)	(23.4)	23.6 ± 0.6	(23.1)	23.7 ± 0.6	(23.4)	22.2 ± 0.7	23.1 ± 0.5	22.8 ± 0.7	23.3 ± 0.5
16	23	11	(24.0)	(24.0)	23.7 ± 0.7	(23.4)	24.0 ± 0.7	(23.7)	22.5 ± 0.8	23.3 ± 0.5	23.4 ± 0.9	24.0 ± 0.7
17	23	19	(23.9)	(23.4)	23.9 ± 0.7	(23.3)	24.0 ± 0.7	(23.9)	22.7 ± 0.9	23.6 ± 0.6	23.3 ± 0.8	23.7 ± 0.6
Error [%]	Bar I		61.1	56.3	49.1	57.2	51.6	68.8	51.8	36.9	51.9	50.5
Region B												
18	27	34	22.6 ± 0.7	22.2 ± 0.7	22.3 ± 0.3	21.5 ± 0.7	22.3 ± 0.3	21.7 ± 0.6	19.4 ± 0.2	20.9 ± 0.2	20.8 ± 0.3	22.4 ± 0.3
19	13	8	(23.5)	(22.8)	22.7 ± 0.4	(22.3)	22.6 ± 0.4	21.8 ± 0.6	19.7 ± 0.2	21.0 ± 0.2	20.9 ± 0.3	22.2 ± 0.3
20	22	12	(23.7)	(23.1)	23.3 ± 0.6	22.2 ± 1.0	23.2 ± 0.5	22.3 ± 0.8	19.9 ± 0.2	21.5 ± 0.2	21.3 ± 0.3	22.8 ± 0.4
21	29	34	22.1 ± 0.5	21.6 ± 0.6	21.6 ± 0.2	21.4 ± 0.7	21.6 ± 0.2	21.5 ± 0.5	20.0 ± 0.3	21.0 ± 0.2	21.0 ± 0.3	21.5 ± 0.2
22	19	34	(23.4)	(22.8)	22.7 ± 0.4	21.9 ± 0.9	22.8 ± 0.4	22.1 ± 0.7	20.0 ± 0.3	21.4 ± 0.2	21.2 ± 0.3	22.5 ± 0.4
23	35	30	23.0 ± 0.8	22.3 ± 0.8	22.8 ± 0.4	21.6 ± 0.8	22.6 ± 0.3	21.9 ± 0.6	20.4 ± 0.3	21.5 ± 0.2	21.3 ± 0.3	22.2 ± 0.3
24	34	30	23.1 ± 0.8	22.5 ± 0.8	22.9 ± 0.4	21.8 ± 0.8	23.1 ± 0.4	22.2 ± 0.7	20.3 ± 0.3	21.7 ± 0.2	21.5 ± 0.3	22.9 ± 0.4
25	53	30	22.9 ± 0.8	22.3 ± 0.8	22.5 ± 0.4	(22.2)	22.3 ± 0.3	21.8 ± 0.6	19.8 ± 0.2	21.3 ± 0.2	21.2 ± 0.3	22.2 ± 0.3
26	40	32	23.0 ± 0.8	22.7 ± 0.9	23.2 ± 0.5	(22.1)	23.1 ± 0.4	22.4 ± 0.8	20.4 ± 0.3	21.8 ± 0.3	21.7 ± 0.4	23.2 ± 0.4
Error [%]	Region B		67.9	70.6	38.1	75.4	34.3	60.3	23.1	19.5	28.6	31.5

NOTE—Columns 2 and 3 give the number of pixels in each aperture (N_{ap}) and in the associated sky region (N_{sky}).

Non-detections, i.e. observations with fractional error $\geq 100\%$, are treated as upper limits and the 1σ value is instead given in parentheses. Symmetric magnitude errors are shown. Symmetric errors of 0.6, 0.8, 1.0 mag correspond to actual, non-symmetric errors of $^{+0.9}_{-0.5}$, $^{+1.4}_{-0.6}$, $^{+2.8}_{-0.7}$ mag, respectively. Galactic reddening correction has been applied. The bottom row of each region shows the average percentage uncertainty (relative error in per cent) for each filter.

Aperture corrections for each filter and each cluster were obtained with `pysynphot`, by assuming that the correction for the corresponding pixel aperture is equivalent to that of a circular aperture with radius $r = \sqrt{\text{area}/\pi}$. These corrections account for variations in the point spread function (PSF) in the different filters, although due to the non-circular geometry of the pixel apertures, these corrections may be somewhat overestimated. Further, all photometry has been corrected for Galactic extinction. The [Schlafly & Finkbeiner \(2011\)](#) reddening curve was used for all *HST* filters redwards of

F336W. For the F125LP and F140LP filters we instead used the [Sasseen et al. \(2002\)](#) FUV attenuation curve.

Table 2. Cluster SED parameters from Cigale fits.

ID	Age (Myr)	f_{esc}	$E(B - V)$ (mag)	$Q(H^0)$ (10^{52} s^{-1})	M_{\star} ($10^7 M_{\odot}$)	χ^2_{ν}
Region A						

Table 2 continued

Table 2 (*continued*)

ID	Age (Myr)	f_{esc}	$E(B - V)$ (mag)	$Q(\text{H}^0)$ (10^{52} s^{-1})	M_* ($10^7 M_\odot$)	χ^2_ν
1	4^{+2}_{-0}	$0.95^{+0.00}_{-0.10}$	$0.05^{+0.01}_{-0.05}$	$151.02^{+9.39}_{-114.03}$	$6.56^{+0.41}_{-0.82}$	0.64
2	12^{+7}_{-1}	$0.95^{+0.00}_{-0.95}$	$0.00^{+0.02}_{-0.00}$	$3.45^{+1.00}_{-2.77}$	$12.16^{+7.89}_{-1.86}$	0.98
3	2^{+2}_{-0}	$0.80^{+0.05}_{-0.30}$	$0.18^{+0.04}_{-0.09}$	$76.85^{+24.60}_{-59.71}$	$2.77^{+0.89}_{-2.02}$	0.32
4	2^{+1}_{-0}	$0.75^{+0.00}_{-0.10}$	$0.21^{+0.01}_{-0.03}$	$64.71^{+3.75}_{-16.44}$	$2.33^{+0.14}_{-0.59}$	0.18
5	2^{+1}_{-0}	$0.80^{+0.00}_{-0.00}$	$0.16^{+0.02}_{-0.01}$	$76.60^{+8.51}_{-4.13}$	$2.76^{+0.31}_{-0.15}$	0.24
6	4^{+0}_{-0}	$0.35^{+0.10}_{-0.20}$	$0.10^{+0.02}_{-0.02}$	$8.99^{+1.81}_{-1.89}$	$0.39^{+0.08}_{-0.08}$	0.16
7	2^{+1}_{-0}	$0.90^{+0.00}_{-0.05}$	$0.18^{+0.02}_{-0.03}$	$23.44^{+2.87}_{-4.97}$	$0.84^{+0.10}_{-0.18}$	0.10
Bar I						
8	2^{+1}_{-0}	$0.75^{+0.00}_{-0.00}$	$0.32^{+0.00}_{-0.00}$	$105.82^{+0.00}_{-0.00}$	$3.81^{+0.00}_{-0.00}$	0.01
9	2^{+1}_{-0}	$0.90^{+0.00}_{-0.00}$	$0.20^{+0.01}_{-0.01}$	$4.79^{+0.29}_{-0.27}$	$0.17^{+0.01}_{-0.01}$	0.02
10	2^{+1}_{-0}	$0.80^{+0.00}_{-0.10}$	$0.23^{+0.03}_{-0.03}$	$4.25^{+0.82}_{-1.03}$	$0.15^{+0.03}_{-0.04}$	0.05
11	12^{+0}_{-1}	$0.95^{+0.00}_{-0.95}$	$0.14^{+0.01}_{-0.04}$	$0.07^{+0.02}_{-0.01}$	$0.23^{+0.01}_{-0.07}$	0.04
12	11^{+1}_{-1}	$0.00^{+0.90}_{-0.00}$	$0.09^{+0.04}_{-0.03}$	$0.02^{+0.01}_{-0.00}$	$0.04^{+0.02}_{-0.01}$	0.04
13	2^{+1}_{-0}	$0.80^{+0.10}_{-0.05}$	$0.22^{+0.05}_{-0.04}$	$3.97^{+1.67}_{-1.02}$	$0.14^{+0.06}_{-0.04}$	0.25
14	2^{+1}_{-0}	$0.85^{+0.00}_{-0.00}$	$0.35^{+0.02}_{-0.01}$	$7.51^{+0.93}_{-0.43}$	$0.27^{+0.03}_{-0.02}$	0.01
15	4^{+14}_{-2}	$0.95^{+0.00}_{-0.95}$	$0.27^{+0.11}_{-0.13}$	$2.08^{+7.45}_{-2.08}$	$0.09^{+0.25}_{-0.02}$	0.06
16	2^{+1}_{-0}	$0.95^{+0.00}_{-0.00}$	$0.29^{+0.01}_{-0.02}$	$4.81^{+0.30}_{-0.54}$	$0.17^{+0.01}_{-0.02}$	0.03
17	12^{+7}_{-0}	$0.15^{+0.80}_{-0.15}$	$0.08^{+0.02}_{-0.02}$	$0.02^{+0.00}_{-0.01}$	$0.06^{+0.05}_{-0.01}$	0.03
Region B						
18	2^{+1}_{-0}	$0.70^{+0.00}_{-0.05}$	$0.27^{+0.02}_{-0.02}$	$13.72^{+1.60}_{-2.19}$	$0.49^{+0.06}_{-0.08}$	0.05
19	2^{+1}_{-0}	$0.70^{+0.05}_{-0.05}$	$0.38^{+0.04}_{-0.02}$	$19.44^{+6.40}_{-3.03}$	$0.70^{+0.23}_{-0.11}$	0.09
20	2^{+2}_{-0}	$0.50^{+0.15}_{-0.50}$	$0.34^{+0.07}_{-0.09}$	$6.99^{+5.09}_{-5.33}$	$0.25^{+0.18}_{-0.18}$	0.08
21	2^{+2}_{-0}	$0.95^{+0.00}_{-0.05}$	$0.34^{+0.00}_{-0.09}$	$46.63^{+0.15}_{-35.93}$	$1.68^{+0.01}_{-1.21}$	0.02
22	2^{+1}_{-0}	$0.80^{+0.00}_{-0.05}$	$0.35^{+0.02}_{-0.03}$	$15.87^{+1.95}_{-3.26}$	$0.57^{+0.07}_{-0.12}$	0.06
23	4^{+0}_{-0}	$0.65^{+0.05}_{-0.40}$	$0.33^{+0.03}_{-0.06}$	$5.85^{+1.26}_{-2.47}$	$0.25^{+0.05}_{-0.11}$	0.13
24	2^{+1}_{-0}	$0.70^{+0.05}_{-0.20}$	$0.25^{+0.05}_{-0.05}$	$6.31^{+2.55}_{-2.43}$	$0.23^{+0.09}_{-0.09}$	0.09
25	2^{+1}_{-0}	$0.85^{+0.00}_{-0.05}$	$0.36^{+0.02}_{-0.04}$	$23.67^{+2.68}_{-6.07}$	$0.85^{+0.10}_{-0.22}$	0.07
26	4^{+0}_{-0}	$0.35^{+0.05}_{-0.10}$	$0.16^{+0.01}_{-0.02}$	$1.34^{+0.13}_{-0.18}$	$0.06^{+0.01}_{-0.01}$	0.03

NOTE—Uncertainties correspond to the resulting parameter range for models within 20% of the minimum χ^2 .

We carry out pixel photometry because the regions are too crowded to allow for aperture photometry with a fixed radius. Using small apertures to accommodate the small distances between clusters resulted in large, and therefore uncertain, aperture corrections on the order of ~ 1 mag. We also attempted to model each cluster with a 2D Moffat function with ASTROPY (Astropy Collaboration et al. 2013). The model photometry of the brightest clusters was consistent with the pixel photometry within the uncertainties, while the fainter clusters were difficult to model. Our pixel photometry for the clusters is summarized in Table 1.

3.2. Cluster SED modeling

Once the photometry was obtained, we modeled the SED of each cluster with the Cigale software (v 0.11.0, Noll et al. 2009; Serra et al. 2011). The available *HST* filters provide 11 photometry measurements covering the FUV and optical from the 10 filters listed in Section 2,

and one repeated observation in F336W from a separate observing program. Cigale accounts for nebular emission by adding a generic H II region spectrum, which may or may not be representative of the physical conditions in Tol 1247-232. Further, the nebular emission in each cluster aperture may be due to ionizing sources outside of the aperture. For these reasons, we treat the narrowband photometry as upper limits during the SED fitting. In addition, to account for the possibility that the narrowband photometry underestimates the flux in the emission lines due to escape of ionizing photons beyond the aperture, the f_{esc} parameter was allowed to vary between 0.0 and 1.0 in 0.05 steps for each cluster. We chose a Salpeter (Salpeter 1955) initial mass function (IMF) with $0.6 \leq M \leq 120M_\odot$, and a constant metallicity of $Z = 0.004$. This metallicity is consistent with that measured for Tol 1247-232 by Terlevich et al. (1993), who used the so-called “direct” method based on the determination of the electron temperature via detection of the temperature-sensitive [O III] line at $\lambda 4363 \text{ \AA}$. We further assumed a quasi-instantaneous star formation history (SFH) in the form of a delayed decreasing exponential with time $t \times e^{-t/\tau_{\text{SFH}}}$, adopting a very short characteristic timescale $\tau_{\text{SFH}} = 0.01$ Myr. During the fit, the age of the stellar population was allowed to vary from 2 to 100 Myr, in steps of 1 Myr, which is the smallest step size allowed by Cigale. The ionization parameter was allowed to take on values of $-4 \leq \log U \leq -1$ in steps of -0.1 . The Calzetti et al. (2000) dust attenuation law was used to fit the internal $E(B - V)$, which was allowed to vary from 0.0 to 0.7 in steps of 0.01. Due to lack of IR data with sufficient resolution, we cannot constrain the dust emission for the clusters, and therefore the assumed fraction of ionizing photons absorbed by dust, f_{dust} , is set to 0.0 and kept constant during the fit. Therefore the individual cluster escape fractions f_{esc} in Table 2 are an upper limit, in the absence of any dust inside of the H II regions.

To break the age-extinction degeneracy, Fouesneau et al. (2012) recommend using an H α filter in addition to broadband *UBVI* filters. Our cluster detection criteria therefore required a $\geq 1\sigma$ detection in *UBVR* and the H α filter. Table 1 lists the average percentage uncertainty for all regions and all filters. Region A is the brightest, strongly dominated by Clusters 1 and 2, followed by Region B and Bar I. The latter contains some of the faintest clusters in the sample. We are predominantly interested in Region A, since it dominates the ionization budget of the galaxy, as we will show in Section 4. The uncertainties in all 10 filters are here on average $\leq 30\%$, and hence the SED is well constrained. For Region B and Bar I, the average uncertainties are $\lesssim 38\%$ and 52% , respectively, for the optical broadband and the H α filters. In the FUV, Region B and Bar I are not as well constrained, with $\lesssim 71\%$ uncertainty and several non-detections among the clusters. The situation is similar for both of these regions for the narrowband filters FR388N ([O II]) and FQ508N (H β). The large un-

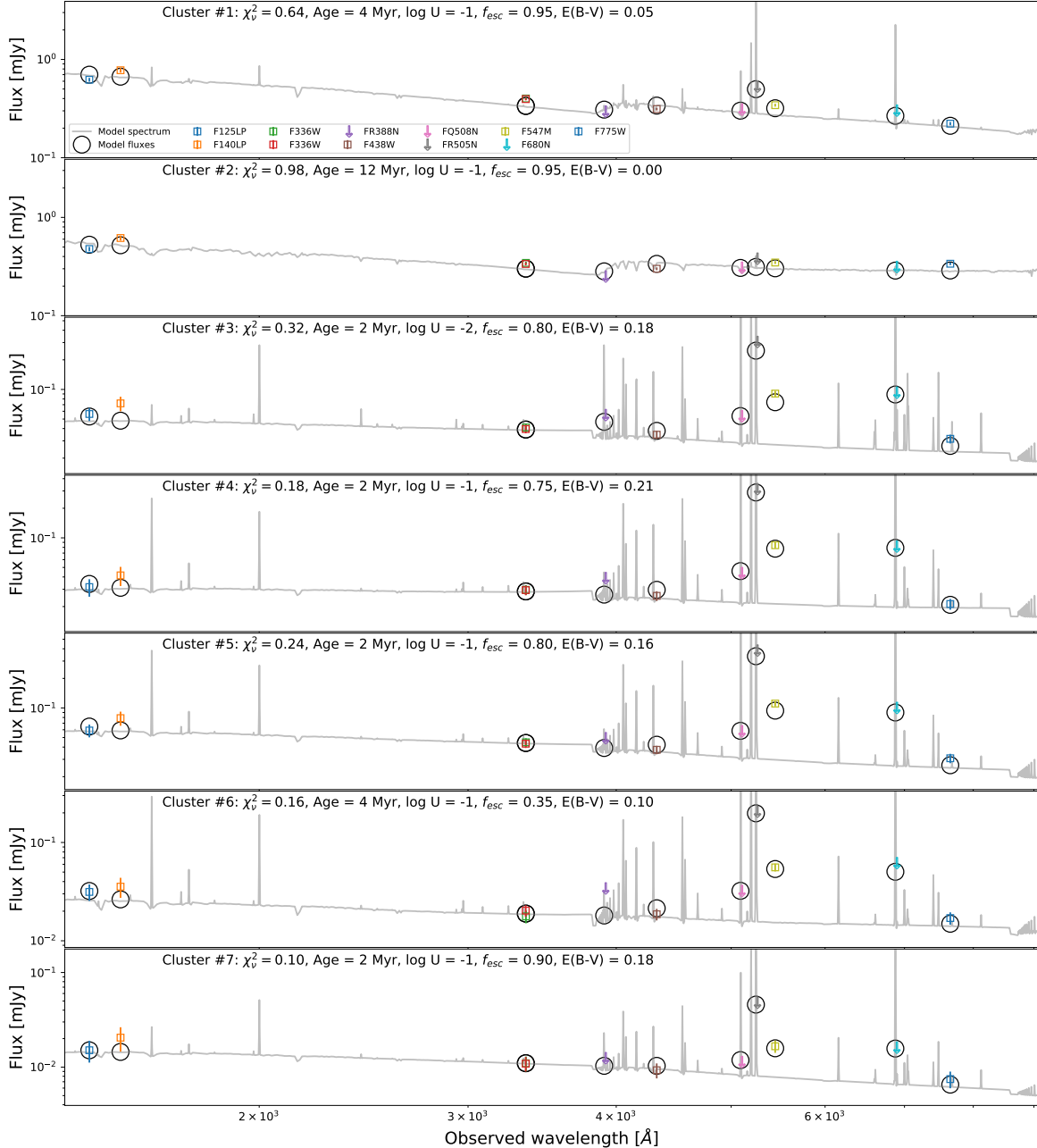


Figure 6. Cigale SED fits for Region A. Photometric data are shown with circles, upper limits are indicated by arrows.

certainties in these filters are of little consequence, since we use all narrowband photometry as upper limits in the SED fits, as described above. For Regions A and B we can test the robustness of our results by also performing SED fits using only the broadband data, which include two FUV filters, and thus one can still break the age-extinction degeneracy without the $H\alpha$ filter. Within the uncertainties, the results were consistent with the SED fits using all available filters (FUV, optical broad- and narrowbands), and we therefore proceed with the SED fits using all filters.

Table 2 shows the major parameters from the best fit models, namely age, $E(B - V)$, f_{esc} , production rate of

ionizing photons $Q(H^0)$, and stellar mass M_* . In Figure 6 we show the corresponding best SED fits for Region A, while Figures B1 and B2 of the Appendix show the SED fits for the remaining clusters in Bar I and Region B, respectively. The upper (lower) uncertainties on the presented parameters are simply the difference between the parameter value at minimum χ^2 and the maximum (minimum) value of the parameter range obtained from all models with χ^2 within 20% of the minimum. This is illustrated in Figures B3 and B4 of the Appendix for the age and f_{esc} parameters, respectively.

We note several things about the SED fits and their uncertainties. First, in some cases the maximum prob-

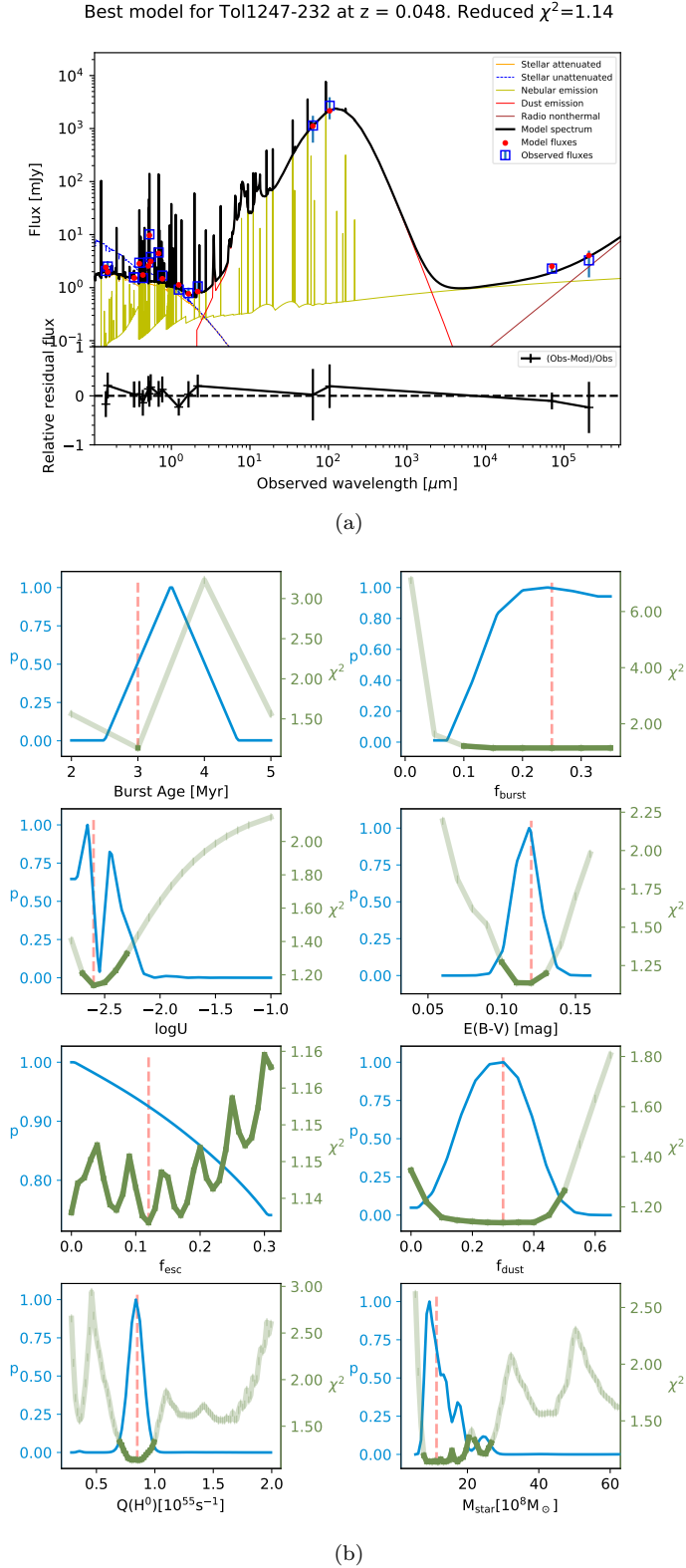


Figure 7. (a) Log plot of Cigale SED fit of Tol 1247–232, with fit components as shown in the legend. (b) PDFs of the major fitted parameters, burst age, young mass fraction, f_{burst} , $\log U$, $E(B - V)$, f_{esc} , f_{dust} , $Q(\text{H}^0)$, and M_* . The PDFs are color-coded in blue, labeled on the left y -axes; the χ^2 distributions are color-coded in green, labeled on the right y -axes. The best model values selected by Cigale, corresponding to the lowest χ^2 , are marked by dashed red lines. χ^2 values within 20% of this minimum represent models indistinguishable from the best fit, and are marked by dark green.

ability does not correspond to the minimum χ^2 as seen in Figures B3 and B4. This is expected, because in each parameter bin, the probability is a weighted sum, evaluated over the χ^2 values of all models in that bin. Therefore, while the best model is in the minimum χ^2 bin, other bins may contain several good models, which may increase their probability enough to offset the peak of the probability density function (PDF) (Noll et al. 2009). Second, Cigale computes the reduced chi-square statistic, χ_ν^2 , where ν is the number of degrees of freedom, and $\chi_\nu^2 = \chi^2/\nu$. In principle, $\chi_\nu^2 > 1$ indicates either that the error variance of the data has been underestimated or that the model is not fully capturing the data, while $\chi_\nu^2 < 1$ indicates either that the model is fitting noise or that the error variance has been overestimated (e.g. Bevington 1969). The latter is likely the reason for the models with $\chi_\nu^2 < 1$ in Table 2 and Figures B3 and B4, since Cigale cannot be fitting noise in our setup. Third, even though Cigale selects a best value for a given parameter, that value may be poorly constrained. Examination of the PDF and χ^2 distribution is invaluable in identifying such cases. For four clusters in Table 2 (Clusters 2, 11, 12, 17) the escape fraction parameter is unconstrained, with possible values covering 0 – 100% escape. To illustrate the stability of the model parameters, we show the PDF and χ^2 distributions for the age and the escape fraction in Figures B3 and B4. Lastly, Cigale is designed primarily for stellar population synthesis modeling of integrated galaxy populations, rather than individual clusters. Since the distribution of nebular light associated with individual clusters corresponds poorly to the spatial apertures of the clusters, nebular parameters such as $\log U$ fitted by Cigale are not meaningful, and therefore not presented in Table 2.

3.3. Galaxy SED modeling

For the 26 clusters we have used only FUV and optical data, because these data have the spatial resolution to separate individual ionizing sources. For the SED of the entire galaxy we can use integrated values from observations with lower resolution, namely, the photometry of the integrated galaxy area in the near-infrared (NIR) J , H , and K_s bands from the 2MASS catalog, in the infrared (IR) at 60 and $100\mu\text{m}$ from the IRAS catalog, and at 1.49 GHz and 4.8 GHz in the radio from Rosa-González et al. (2007). To obtain the integrated FUV and optical photometry of the entire galaxy we performed aperture photometry on all FUV and optical images, with a radius of 5.8 arcsec, as indicated in Figure 2a. Since we are now evaluating the entire stellar population of Tol 1247–232, we assumed a double exponential SFH law, with one exponential for the young population, and one for the underlying old population. We assumed an old population of 6 Gyr, with a short e -folding time $\tau_{\text{old}} = 0.01$ Myr. For the superimposed young population, we assumed an equally short e -folding time $\tau_{\text{burst}} = 0.01$ Myr, and varied the young mass frac-

tion f_{burst} between 0.01 and 0.35 in steps of 0.05, and the burst age between 2 to 20 Myr in steps of 1 Myr. In addition to these, the $\log U$, f_{esc} , f_{dust} and $E(B-V)$ parameters were also varied with the same range as for the

clusters. The best model parameters are listed in Table 3, with the SED displayed in Figure 7a. The PDF of the major parameters and the minimum χ^2_{ν} are shown in Figure 7b.

Table 3. Tol 1247-232 SED parameters from Cigale fits, using a double exponential SFH.

ID	Burst Age (Myr)	f_{burst}	$\log U$	f_{esc}	f_{dust}	$E(B-V)$	$Q(\text{H}^0)$ (10^{54} s^{-1})	M_{\star} ($10^9 M_{\odot}$)	χ^2_{ν}
Tol 1247 – 232	3_{-0}^{+0}	$0.25_{-0.15}^{+0.10}$	$-2.6_{-0.1}^{+0.3}$	$0.12_{-0.12}^{+0.19}$	$0.3_{-0.3}^{+0.2}$	$0.12_{-0.02}^{+0.01}$	$8.49_{-1.60}^{+1.36}$	$1.13_{-0.40}^{+1.53}$	1.14

NOTE—Uncertainties correspond to the resulting parameter range for models within 5% of the minimum χ^2 .

The IR data constrain the dust content and we can therefore fit the fraction of ionizing photons absorbed by dust, f_{dust} . For the best model, and models with similar χ^2_{ν} , $f_{\text{dust}} = 0.3_{-0.3}^{+0.2}$. Typical fractions of dust-absorbed LyC photons are $\sim 50\%$ for solar and LMC metallicities (Inoue 2001). The lower, SMC-like, metallicity of Tol 1247–232 is consistent with f_{dust} fractions being somewhat lower here, although within the uncertainties, f_{dust} is also consistent with fractions for solar and LMC metallicities. We obtain a dust attenuation of $E(B-V) = 0.12_{-0.02}^{+0.01}$, which is consistent with estimates from observed Balmer line ratios ($E(B-V) = 0.13$; Puschnig et al. 2017) and with modeling the SED by fitting the observed FUV COS spectrum ($E(B-V) = 0.11$; Leitherer et al. 2016).

Within the uncertainties, the resulting stellar mass $1.13_{-0.40}^{+1.53} \times 10^9 M_{\odot}$ is a factor of 2.2 from the estimate by Leitert et al. ($5.9 \times 10^9 M_{\odot}$; 2013), who obtained the stellar mass by simply assuming a reasonable mass-to-light ratio based on the statistical average of local SFGs, and hence their estimate can certainly be off by a factor of 2-3. Comparing our mass to the total mass of all clusters in Table 2, we find that the young mass fraction is $\sim 34\%$, which is consistent within the errorbars with the value found by Cigale. This young population gives a total production rate of ionizing photons $Q(\text{H}^0)_{\text{total}} = 8.5 \times 10^{54} \text{ s}^{-1}$. From these, a fraction of 0.42 are absorbed by dust and/or escape (Table 3), and the remaining $Q(\text{H}^0)_{\text{ion}} = 4.9 \times 10^{54}$ photons per second are left to ionize the gas. Note, that the escape fraction is unconstrained, in the sense that all values below 0.31 are consistent with the best model (Table 3).

3.4. Classical WR or VMS Stars?

Wolf-Rayet (WR) stars in Tol 1247–232 have been reported by Masegosa et al. (1991) and confirmed by Schaerer et al. (1999) through re-analysis of the same data. Classical WR stars of the carbon (WC) and nitrogen (WN) sequences are the stripped cores of evolved massive stars. Their strong stellar winds provide substantial mechanical feedback, and they can be used to age-date stellar clusters, implying an age of ~ 5 Myr

(e.g., Crowther 2007). WN stars can be inferred from the so-called “blue bump” due to broad He II $\lambda 4686$ emission, while WC stars will display a “red bump” at $\lambda 5810 \text{ \AA}$.

An alternative explanation to the “blue bump” may be very massive stars (VMS). Young VMS are known to also show WN spectral features (e.g. Crowther et al. 2010; Crowther & Walborn 2011; Gräfenor & Vink 2015; Smith et al. 2016). VMS O-type stars have been detected in the LMC SSC R136, a very massive and extremely young cluster ($M \geq 10^4 M_{\odot}$, ≤ 2 Myr; Crowther et al. 2010). A similar situation has been suggested in Mrk 71 (James et al. 2016; Micheva et al. 2017), where VMS could explain the detection of broad He II and are consistent with the ~ 1 Myr age of its dominant SSC, Knot A. The SED models in our analysis cannot differentiate ages ≤ 3 Myr, and some of the clusters in Tol 1247–232 could be even younger than what we have indicated in Table 2. It is therefore possible that the observed WN spectral features are due to VMS stars in SSCs of extremely young ages ~ 1 Myr in this galaxy.

The presence of WC stars would support the interpretation of a classical WN population. We evaluated the possibility of WC stars by re-examining the available spectra. There are two optical spectra of Tol 1247–232 from the ESO 3.6m and the Las Campanas DuPont telescopes, published in the H II galaxy catalog of Terlevich et al. (1991), and used to detect the blue bump in Masegosa et al. (1991) and Schaerer et al. (1999). These data were kindly provided to us by R. J. Terlevich. Due to the low resolution of the ESO spectrum, and a second order contamination of the DuPont spectrum (R. J. Terlevich, private communication), we are unable to definitively exclude the presence of the $\lambda 5810 \text{ \AA}$ red bump and implied WC stars. If a red bump is present in these spectra, it is below the detection limit. Therefore, the WR stars in Tol 1247–232 are likely dominated by WN type, and the possibility of VMS cannot be discarded.

Cigale assumes a “standard” population of single stars with masses $0.6 \leq M \leq 120 M_{\odot}$ and no binary companions. There is evidence in the literature that accounting for binary evolution improves the agreement between ob-

servations and synthetic spectra (e.g. Eldridge & Stanway 2009; Eldridge & Relaño 2011). In such models, WR stars can manifest over a wider age range, which boosts the UV flux and the LyC production of their host galaxy. Our predictions for the cluster production rates of ionizing photons may therefore be underestimated.

4. LYMAN CONTINUUM ESCAPE

In Section 2.2 and Figure 4a, IPM based on the [O III] and [O II] lines revealed a large area of ionized, optically thin gas. This area includes the entire central Region A (2.3 kpc in diameter), and extending well beyond the stellar body of the galaxy to the northwest and southeast of Region A, reaching ~ 3 kpc in both directions from the center. Clusters 1 and 2 in Region A are the most massive and the brightest objects in the entire galaxy in both FUV and optical (Table 1), and are separated by a projected distance of 280 pc. Outside of Region A, the brightest object is Cluster 8 in Bar I, which is the third most massive cluster in the galaxy, and on average as bright as some of the Region A clusters. These three clusters alone cannot account for all of the observed ionized gas. In what follows, we examine the contribution of all 26 clusters to the ionization structure of the ISM. We note that the stellar mass in all apertures is between 10^5 and $10^8 M_\odot$, as seen in Table 2. This means that our clusters are either a congregation of clusters or an individual SSC.

We estimate the fraction of diffuse gas emission in Tol 1247–232, which we define as the fraction of the total nebular flux outside of the apertures for the 26 clusters in Table 2. We use the pixel photometry in Table 1 to represent the radiation coming from the clusters and their immediate vicinity. To obtain the emission-line fluxes within the apertures, we use the continuum-subtracted images obtained in Section 2.1. For the total nebular flux of the galaxy in each of the narrowband filters, we use the same fixed aperture of $r = 5.8$ arcsec. The diffuse emission is then estimated as the fraction of flux outside of the object apertures.

For [O II], H β , [O III], and H α , we obtain diffuse fractions of 0.83, 0.89, 0.76, and 0.83, respectively. These fractions are much higher than typical warm interstellar medium (WIM) fractions for starburst galaxies, which are around ~ 20 per cent (Oey et al. 2007). This is because our definition of the diffuse radiation differs from conventional WIM analysis, in particular, that our cluster apertures are defined by the stellar light and therefore are much smaller, excluding the outer areas of the H II regions associated with each cluster. Our diffuse radiation fraction of 0.83 in H α is consistent with Östlin & the LARS team (2016), who model the H α emission in Tol 1247–232 pixel by pixel and estimate the diffuse fraction in a similar fashion.

Balancing the budget of intrinsic and observed ionizing photons, one can use the diffuse radiation fraction, and the modeled $Q(\text{H}^0)$ and f_{esc} from Table 2 to estimate the global escape fraction of ionizing photons.

From the SED fit to the entire galaxy, in Section 3.3 we obtained $Q(\text{H}^0)_{\text{ion}} = 4.9 \times 10^{54} \text{ s}^{-1}$. With an average diffuse fraction of 0.83, this corresponds to a production rate of diffuse ionizing photons of $Q(\text{H}^0)_{\text{diffuse}} = 4.1 \times 10^{54} \text{ s}^{-1}$. This is the ionizing photon emission rate that the ionizing sources in the galaxy must account for, and any excess above this number will escape into the IGM. From all 26 clusters, the rate of ionizing photons, escaping into the ISM is $\sum Q(\text{H}^0)_i \times f_{\text{esc},i} = 5.6 \times 10^{54} \text{ s}^{-1}$, where $Q(\text{H}^0)_i$ and $f_{\text{esc},i}$ are obtained from Table 2, using parameter values at minimum χ_ν^2 . This implies that the radiation leaking from the clusters into the ISM can account for $1.37 \times Q(\text{H}^0)_{\text{diffuse}}$, and hence the global escape fraction is 0.27. Using the maximum parameter values from Table 2 (positive errorbars), the 26 clusters can account for $1.55 \times Q(\text{H}^0)_{\text{diffuse}}$, and the global escape fraction is 0.35. Using the minimum parameter values from Table 2 (negative errorbars), the 26 clusters can account for only $0.73 \times Q(\text{H}^0)_{\text{diffuse}}$, and hence the global escape fraction is zero. We further note that taking the SED models at minimum χ_ν^2 at face value, Region A (Clusters 1 – 7) dominates the production of ionizing photons, and alone accounts for $0.83 \times Q(\text{H}^0)_{\text{diffuse}}$.

The above estimates for the global f_{esc} are obtained by ignoring dust absorption inside the H II regions. From the SED modeling of the entire galaxy in Section 3.3, we obtained a model value for the fraction of ionizing photons absorbed by dust, f_{dust} . The global LyC escape fraction can then be expressed as,

$$f_{\text{esc}}^{\text{galaxy}} = 1 - \frac{Q(\text{H}^0)_{\text{obs}}}{(1 - f_{\text{dust}}) \times \sum_{i=1}^{26} Q(\text{H}^0)_i}, \quad (1)$$

for the case that $\sum_{i=1}^{26} Q(\text{H}^0)_i > Q(\text{H}^0)_{\text{obs}}$, and zero otherwise. Here we assume that f_{dust} is a constant effective fraction of absorbed LyC photons that applies to all individual clusters. $Q(\text{H}^0)_{\text{obs}}$ is obtained from the observed H β luminosity of the galaxy, assuming case B recombination, and is estimated to be $Q(\text{H}^0)_{\text{obs}} = 4.2 \times 10^{54} \text{ s}^{-1}$, after correcting for internal extinction with $E(B - V) = 0.11$. $Q(\text{H}^0)_i$ is the model intrinsic LyC production rate from Cluster i , obtained from its Cigale SED fit in Table 2. The dust fraction at minimum χ_ν^2 is $f_{\text{dust}} = 0.30$, as shown in Table 3. With these values one obtains $\sum Q(\text{H}^0)_i = 6.78 \times 10^{54} \text{ s}^{-1}$. From equation 1 the resulting global escape fraction is $f_{\text{esc}}^{\text{galaxy}} = 0.12_{-0.12}^{+0.31}$, which represents the total isotropic escape in all directions, after accounting for dust both in the ISM and inside of the HII regions. The uncertainties on this value are the propagated uncertainties in f_{dust} and $\sum Q(\text{H}^0)_i$ from tables 2 and 3, added in quadrature.

We note that this estimate is sensitive to the individual escape fractions from all clusters, the estimate of the diffuse radiation fraction, the dust absorption fraction, and the modeled intrinsic number of ionizing photons. For example, if the diffuse radiation fraction is $\geq 20\%$ lower, then the minimum $Q(\text{H}^0)_i$ can still account for all diffuse radiation, and result in a non-zero

global escape fraction of $\gtrsim 2\%$. Further, SED models of ages younger than 2 Myr are unavailable in Cigale, and hence we cannot model clusters dominated by extremely young, very massive stars (cf. Section 5) of $\lesssim 1$ Myr. VMS would significantly boost the intrinsic production of $Q(\text{H}^0)_i$ and further boost the escape fraction.

5. DISCUSSION

The observed LyC escape fraction from Tol 1247–232 has been measured several times through direct observations in the LyC regime. It was first detected with $f_{\text{esc}} = 0.024_{-0.008}^{+0.009}$ from *FUSE* data (Leitet et al. 2013). The detection was later confirmed with *HST*/COS data but measured to be $f_{\text{esc}} = 0.045 \pm 0.012$ (Leitherer et al. 2016). Puschig et al. (2017) found a negative flux issue with the COS reduction pipeline and re-measured f_{esc} at 0.015 ± 0.005 . In a third re-analysis of the COS data, Chisholm et al. (2017) claim that the dark current has been significantly underestimated by Leitherer et al. (2016) and instead obtain $f_{\text{esc}} = 0.004 \pm 0.002$. These same authors predict a higher f_{esc} of 0.05 from H I absorption properties in their most recent work (Chisholm et al. 2018), which is consistent with the Leitherer et al. (2016) measurement.

Our global $f_{\text{esc}}^{\text{galaxy}} = 0.12_{-0.12}^{+0.31}$ is higher than these observed measurements, but within the uncertainties, it is also consistent with zero LyC escape, and is therefore in agreement with these previous studies. However, taking our estimate at face value, it is substantially higher than the observed values of f_{esc} . Since the latter are measured in the line of sight, this would suggest that the escape of ionizing radiation is not isotropic, and would depend on viewing angle. This is consistent with the non-isotropic nature of galactic winds and outflows (Veilleux et al. 2005). As described earlier, such mechanical feedback may facilitate LyC escape (e.g., Zastrow et al. 2011, 2013). Non-isotropic escape via ionized “tails”, reaching the outskirts of the galaxy, has also been suggested for the low-metallicity star-forming galaxy SBS 0335-52E (Herenz et al. 2017).

The highly disturbed and irregular morphology of Tol 1247–232, seen in Figure 2a, suggests a major merger event, typical of starbursts that are candidate LCEs. Our SED analysis indicates the presence of at least two young populations of ≤ 4 and ~ 12 Myr age (Table 2), likely the product of star formation triggered by the merger. The SED modeling also indicates that clusters in Region B and Bar I appear to be much dustier than those in the central Region A, with average $E(B - V) = 0.32, 0.18,$ and $0.12,$ respectively, as seen in Table 2. Since one does not expect the average dust attenuation to increase towards the outskirts of a galaxy, the high $E(B - V)$ values in Region B and Bar I suggest that they may be remnants of the main bodies of the progenitor merging galaxies.

In an interacting merger system, mechanical feedback from intense star formation is expected to play a significant role in sculpting the morphological structure of

the ISM. Evidence of mechanical feedback can be observed in the morphology of the ionized gas, traced by nebular emission. The continuum-subtracted H α line image in Figure 8 highlights numerous loops, filaments and cavities. These structures have scales on the order of ~ 1 kpc, and therefore require multiple episodes of star formation (e.g., Chu 2008). The two loops and the northwest cavity, indicated in the figure, could be multi-supernova superbubbles. Note the symmetric geometry centered on Cluster 2, comprising the two cavities directly above and below the cluster. In this projection, the cavities are perpendicular to the galaxy axis, bisecting Region B and the central Region A. These structures apparently correspond to ionized gas, outlined by filamentary strands of nebular emission, and lack any substantial stellar component.

We can compare the stellar population and morphology of optically thin regions in Tol 1247–232 with what is seen in other starburst galaxies. The IPM studies of NGC 5253 and NGC 3125 revealed narrow ionization cones, most likely powered by clusters between 1-5 Myr of age (Zastrow et al. 2011, 2013). These works point out the presence of older stellar populations with ages 10-100 Myr from prior star-formation episodes in both galaxies, and suggest that the ionization cones formed through low density channels pre-cleared by the older clusters. This is supported by the apparently preferred orientation of the ionization cones perpendicular to the major axis of these galaxies (Zastrow et al. 2013). The age distribution of the clusters in Tol 1247–232 similarly indicate a two-stage starburst (Table 2), where, in addition to the young objects $\lesssim 4$ Myr old, an older population from a previous star formation episode is also present, with average age ~ 12 Myr. The most prominent cluster from this older population is the centrally positioned Cluster 2, which is the most massive object in the entire galaxy, and rivals its neighbor, Cluster 1, in brightness, both in the FUV and optical. However, instead of narrow ionization cones, Tol 1247–232 shows a large, highly extended area of ionized gas (Figure 4a) centered on Region A, which reaches the outskirts of the galaxy to the north-west and south-east. The presence of large-scale, optically thin regions revealed by IPM is consistent with the known LyC emission from this galaxy and confirms the use of this technique in clarifying LyC radiative transfer. Another LCE showing similar, extended, optically thin morphology through IPM is Haro 11 (Keenan et al. 2017), where a broad, optically thin region extends > 1 kpc from the center of Knot A into the outskirts of the galaxy. Interestingly, the star formation history in Haro 11 is also consistent with a two-stage starburst, with a young population of SSCs having ages ~ 3.5 Myr, and an older population having ages $\gtrsim 40$ Myr (Adamo et al. 2010).

Thus, a common feature emerging among galaxies with large-scale optically thin regions with likely LyC escape, is the two-stage starburst, in which the episodes of star-formation are separated by ~ 5 –40 Myr. While

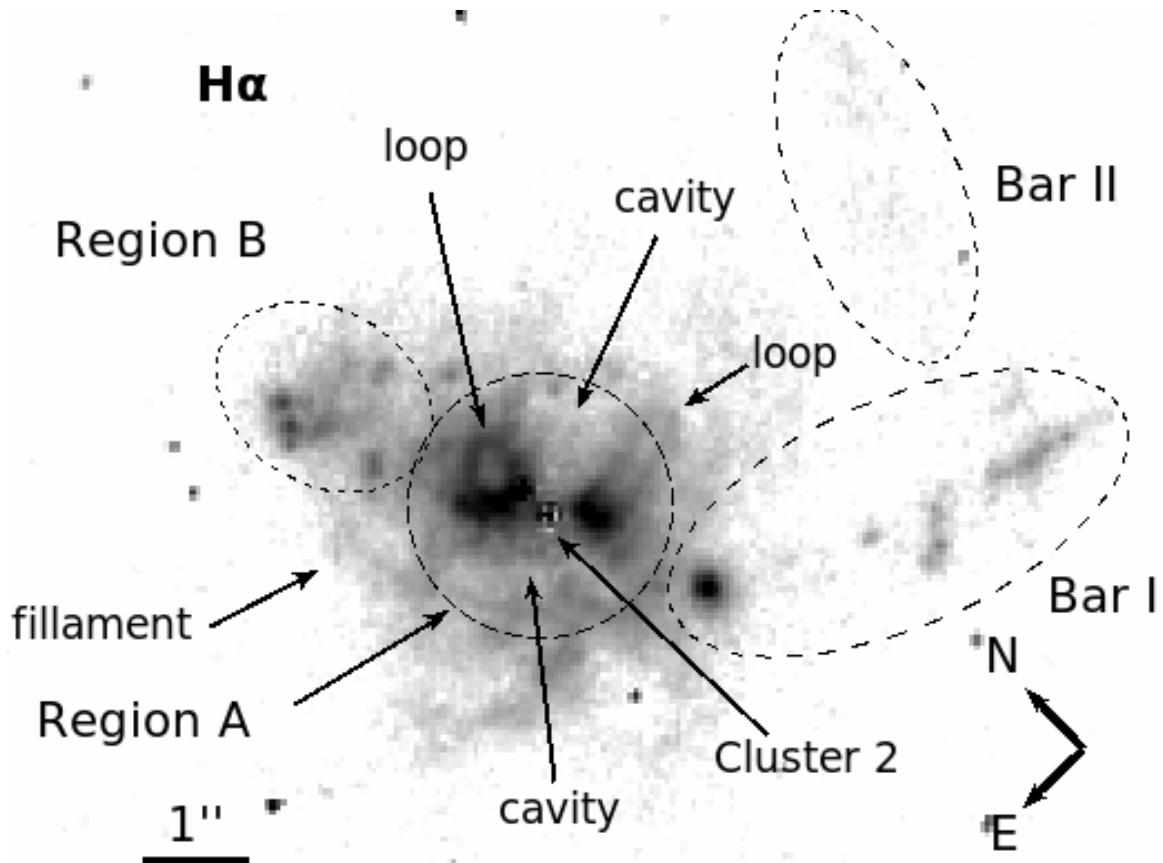


Figure 8. Continuum subtracted $H\alpha$ image, showing the structure of the ionized gas. Several loops and filaments are visible in emission in and around Region A. Regions A, B, Bar I and II are indicated with dashed ellipses for orientation.

narrow ionization cones are seen in the candidate LCEs NGC 5253 and NGC 3125 (Zastrow et al. 2013), the two confirmed LCEs Haro 11 and Tol 1247–232 reveal much more extensive optically thin ISM. It is possible that the morphologies appear different simply due to projection effects, and IPM of larger samples of LCEs are needed to quantitatively characterize the ionization structure in these objects.

We note that X-ray emission from an accreting point source has been detected in both Haro 11 (Prestwich et al. 2015) and in region A of Tol 1247–232 (Rosa González et al. 2009; Kaaret et al. 2017), which may contribute to the LyC escape, and help explain the extremely high ionization parameter of $\log U = -1$, preferred for this galaxy by population synthesis models.

6. CONCLUSIONS

We have used FUV and optical *HST* imaging of Tol 1247–232 to study the ionization structure of this confirmed LCE via the technique of ionization-parameter mapping. The continuum emission in the $[O\ II]\lambda 3727$, $H\beta$, $[O\ III]\lambda\lambda 4959, 5007$, and $H\alpha$ narrowband filters was first subtracted with the mode method of Keenan et al. (2017), and we demonstrated that this method gives continuum scaling factors consistent with the skewness method of Hong et al. (2014) and the pixel-to-pixel method used by, e.g., Böker et al. (1999). IPM using

$[O\ III]$ and $[O\ II]$ reveals a large, optically thin area, engulfing the central region and reaching the outskirts of the galaxy, at ~ 3 kpc from the center along the minor axis. Thus, IPM unambiguously confirms the central region as the origin of the LyC photons that escape in Tol 1247–232.

We identify 26 SSCs, seven of which are located in the central, brightest region of the galaxy, and we model their SEDs with Cigale. Our results from minimum χ^2 SED fitting indicate a population of very young ages of 2–4 Myr for most clusters. The two brightest Clusters, 1 and 2, are located in the central region, and are separated by a projected distance of 280 parsec. The emerging scenario for the escape of LyC in Tol 1247–232 appears to be a two-stage starburst, in which the older Cluster 2 (12 Myr old) has generated large-scale superbubbles, loops, and filaments via mechanical feedback. Young clusters (≤ 4 Myr) from the second star formation episode, dominated by Cluster 1, have then ionized the surrounding ISM, facilitated by this pre-clearing of the region. WN stars have been previously detected in this galaxy, and we highlight the possibility that these may instead be unevolved ($\lesssim 1$ Myr) very massive stars (VMS). Their confirmed presence would revise the age of Cluster 1 accordingly. The LyC luminosity in the central region is so high that large areas appear to be optically thin, not just the lowest-density cavities.

Based on the cluster SED models and observed $H\beta$ emission in Tol 1247–232, we obtain a LyC escape fraction $f_{\text{esc}}^{\text{global}} = 0.12^{+0.31}_{-0.12}$. The central Region A dominates the ionization. The 26 clusters can fully account for the observed ionized ISM, and furthermore can leak LyC with a global non-zero escape fraction. Within the uncertainties, this is consistent with direct measurements of f_{esc} on the order of a few percent in the literature, and also with a zero escape fraction. Our larger estimated value compared to the measurements supports the idea that LyC escape is not isotropic, and may depend on viewing angle.

APPENDIX

A. EFFECTS OF LINE CONTAMINATION IN CONTINUUM FILTERS

The underlying assumption in integrated scaling factor methods is that any emission lines in the continuum filter have a small contribution compared to the total continuum flux, which may not be a justified assumption for starburst galaxies (e.g. Krueger et al. 1995). In our case, F336W, F438W, and F775W do not contain any strong emission lines, while F547M, used for subtracting the continuum from the [O III] narrowband filter FR505N, is affected by the presence of strong [O III] emission. Keenan et al. (2017) test their mode method on synthetic data sets, containing pixels with different continuum and line properties. Their tests reveal that as long as there are some continuum-dominated pixels, the mode method determines the true scaling factor. If no such pixels are present, the scaling factor will be slightly overestimated. In addition, the presence of the [O III] line in the continuum filter will also cause the continuum flux to be overestimated (e.g., Kennicutt et al. 2008). This can lead to an oversubtraction of the continuum and consequently to an underestimation of the [O III] line flux. Following Kennicutt et al. (2008), we estimate that due to the presence of [O III] in the continuum filter, the effective filter transmission at the wavelength of [O III] is lowered by $\sim 80\%$, leading to an underestimate of the [O III] flux by a factor of ~ 5 . We do not apply this correction but note that our [O III]/[O II] ratios are therefore lower limits.

B. COMPARISON OF CONTINUUM SUBTRACTION METHODS

As a sanity check for the mode method of continuum subtraction in Section 2.1, here we compare with the method from Hong et al. (2014), shown in Figure A1a. This method uses the skewness of the pixel flux distribution for the continuum-subtracted image instead of the mode. The optimal scaling factor μ is again found near the transition from undersubtracted to oversubtracted. In the case of continuum-dominated pixels, this transition is marked by a pronounced “bump” in the skewness function. The figure indicates that the μ values obtained from the mode method are in good agreement with the

values suggested by the observed location of the skewness transition bump.

As another check, we also compare with the pixel-to-pixel method (e.g., Böker et al. 1999; Kennicutt et al. 2008) in Figure A1b. This method presents the pixel fluxes in the line filter as a function of their fluxes in the continuum filter. In this representation, continuum-dominated pixels will fall on a straight line, from which a scaling factor can be recovered as the inverse of the slope. In the absence of emission line contribution to the flux, all pixels will fall on linear relation whose slope depends solely on the relative filter shapes. As seen by the excess emission in the line filter, the vast majority of pixels have strong emission-line contributions in all four line filters (Figure A1b). The continuum-dominated pixels form the lower, linear envelope corresponding to the blue dashed line, obtained from converting μ_{mode} from the mode method to a line of the shown slope.

C. SUPPLEMENTARY DATA FROM SED FITS

Figures B1 and B2 show the Cigale SED fits for the clusters of Bar I and Region B, respectively. We show, as examples, output model SED parameters, with the probability density functions (PDF) for age and f_{esc} in Figures B3 and B4, respectively. Light green shows χ^2 , regions with χ^2 within 20% of the minimum χ^2 are indicated by dark green, and the PDF of each parameter with a blue solid line.

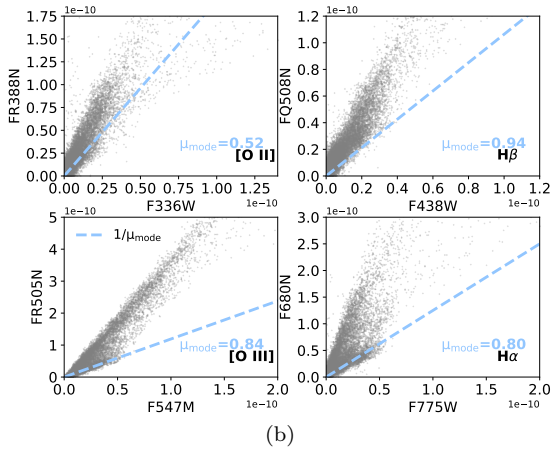
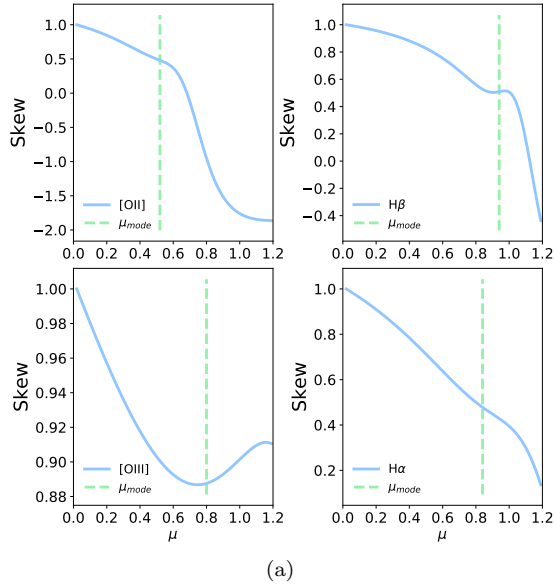


Figure A1. (a) Hong et al. (2014) method: Normalized skewness as a function of scaling factor μ . The scaling factor obtained via the mode method is indicated by a dashed vertical line. (b) Pixel-to-pixel method: Pixel fluxes in the line filter (y -axis) as a function of their fluxes in the continuum filter (x -axis). The scaling factor obtained via the mode method is indicated by a dashed line, and the excess values in the narrow-band filters correspond to nebular emission above the continuum level. All panels are zoomed in to better show the continuum-dominated pixels, found at low flux levels.

We thank the referee, Polychronis Papaderos, for the comments and suggestions, which helped improve this work. The authors are grateful to Göran Östlin for helpful discussions and to Médéric Boquien for offering invaluable advice on the Cigale software. We also thank Roberto Terlevich for sharing the ground-based spectra of this galaxy. This work was supported by NASA grant HST-GO-13702 and the University of Michigan.

REFERENCES

- Adamo, A., Östlin, G., Zackrisson, E., et al. 2010, MNRAS, 407, 870
- Astropy Collaboration, Robitaille, T. P., Tollerud, E. J., et al. 2013, A&A, 558, A33
- Bergvall, N., Zackrisson, E., Andersson, B.-G., et al. 2006, A&A, 448, 513
- Bevington, P. R. 1969, Data reduction and error analysis for the physical sciences
- Böker, T., Calzetti, D., Sparks, W., et al. 1999, ApJS, 124, 95
- Borthakur, S., Heckman, T. M., Leitherer, C., & Overzier, R. A. 2014, Science, 346, 216
- Calzetti, D., Armus, L., Bohlin, R. C., et al. 2000, ApJ, 533, 682
- Cardamone, C., Schawinski, K., Sarzi, M., et al. 2009, MNRAS, 399, 1191
- Chisholm, J., Orlitová, I., Schaerer, D., et al. 2017, A&A, 605, A67
- Chisholm, J., Gazagnes, S., Schaerer, D., et al. 2018, ArXiv e-prints, arXiv:1803.03655
- Chu, Y.-H. 2008, in IAU Symposium, Vol. 250, Massive Stars as Cosmic Engines, ed. F. Bresolin, P. A. Crowther, & J. Puls, 341–354
- Crowther, P. A. 2007, ARA&A, 45, 177
- Crowther, P. A., Schnurr, O., Hirschi, R., et al. 2010, MNRAS, 408, 731

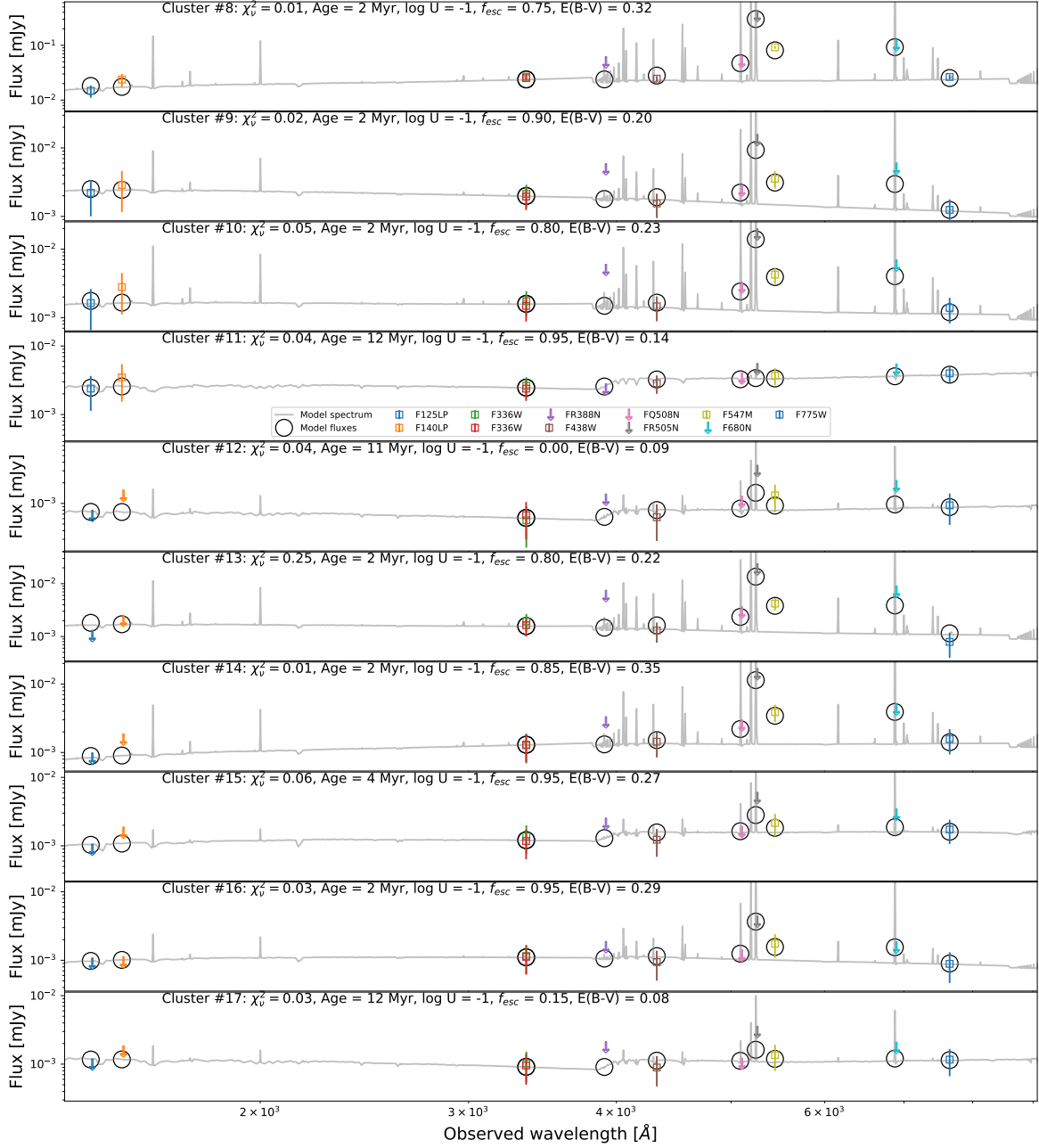


Figure B1. Cigale SED fits for Bar I. Photometric data are shown with circles, upper limits with arrows.

Crowther, P. A., & Walborn, N. R. 2011, MNRAS, 416, 1311
 Eldridge, J. J., & Relaño, M. 2011, MNRAS, 411, 235
 Eldridge, J. J., & Stanway, E. R. 2009, MNRAS, 400, 1019
 Fouesneau, M., Lançon, A., Chandar, R., & Whitmore, B. C. 2012, ApJ, 750, 60
 Gräfener, G., & Vink, J. S. 2015, A&A, 578, L2
 Hayes, M., Östlin, G., Mas-Hesse, J. M., & Kunth, D. 2009, AJ, 138, 911
 Heckman, T. M., Hoopes, C. G., Seibert, M., et al. 2005, ApJL, 619, L35
 Herenz, E. C., Hayes, M., Papaderos, P., et al. 2017, A&A, 606, L11
 Hong, S., Calzetti, D., & Dickinson, M. 2014, PASP, 126, 79
 Inoue, A. K. 2001, AJ, 122, 1788

Izotov, Y. I., Orlitová, I., Schaerer, D., et al. 2016a, Nature, 529, 178
 Izotov, Y. I., Schaerer, D., Thuan, T. X., et al. 2016b, MNRAS, 461, 3683
 Izotov, Y. I., Schaerer, D., Worseck, G., et al. 2018, MNRAS, 474, 4514
 James, B. L., Auger, M., Aloisi, A., Calzetti, D., & Kewley, L. 2016, ApJ, 816, 40
 Jaskot, A. E., & Oey, M. S. 2013, ApJ, 766, 91
 Kaaret, P., Brorby, M., Casella, L., & Prestwich, A. H. 2017, MNRAS, 471, 4234
 Keenan, R. P., Oey, M. S., Jaskot, A. E., & James, B. L. 2017, ApJ, 848, 12
 Kennicutt, Jr., R. C., Lee, J. C., Funes, J. G., et al. 2008, ApJS, 178, 247



Figure B2. Cigale SED fits for Region B. Symbols are as in Figure B1.

- Krueger, H., Fritze-v. Alvensleben, U., & Loose, H.-H. 1995, *A&A*, 303, 41
- Leitet, E., Bergvall, N., Hayes, M., Linné, S., & Zackrisson, E. 2013, *A&A*, 553, A106
- Leitet, E., Bergvall, N., Piskunov, N., & Andersson, B.-G. 2011, *A&A*, 532, A107
- Leitherer, C., Hernandez, S., Lee, J. C., & Oey, M. S. 2016, *ApJ*, 823, 64
- Masegosa, J., Moles, M., & del Olmo, A. 1991, *A&A*, 244, 273
- Micheva, G., Oey, M. S., Jaskot, A. E., & James, B. L. 2017, *ApJ*, 845, 165
- Noll, S., Burgarella, D., Giovannoli, E., et al. 2009, *A&A*, 507, 1793
- Oey, M. S., Meurer, G. R., Yelda, S., et al. 2007, *ApJ*, 661, 801
- Östlin, G., & the LARS team. 2016, *IAU Focus Meeting*, 29, 199
- Overzier, R. A., Heckman, T. M., Tremonti, C., et al. 2009, *ApJ*, 706, 203
- Pellegrini, E. W., Oey, M. S., Winkler, P. F., et al. 2012, *ApJ*, 755, 40
- Prestwich, A. H., Jackson, F., Kaaret, P., et al. 2015, *ApJ*, 812, 166
- Puschnig, J., Hayes, M., Östlin, G., et al. 2017, *MNRAS*, 469, 3252
- Rosa-González, D., Schmitt, H. R., Terlevich, E., & Terlevich, R. 2007, *ApJ*, 654, 226
- Rosa González, D., Terlevich, E., Jiménez Bailón, E., et al. 2009, *MNRAS*, 399, 487
- Salpeter, E. E. 1955, *ApJ*, 121, 161
- Sasseen, T. P., Hurwitz, M., Dixon, W. V., & Airieau, S. 2002, *ApJ*, 566, 267

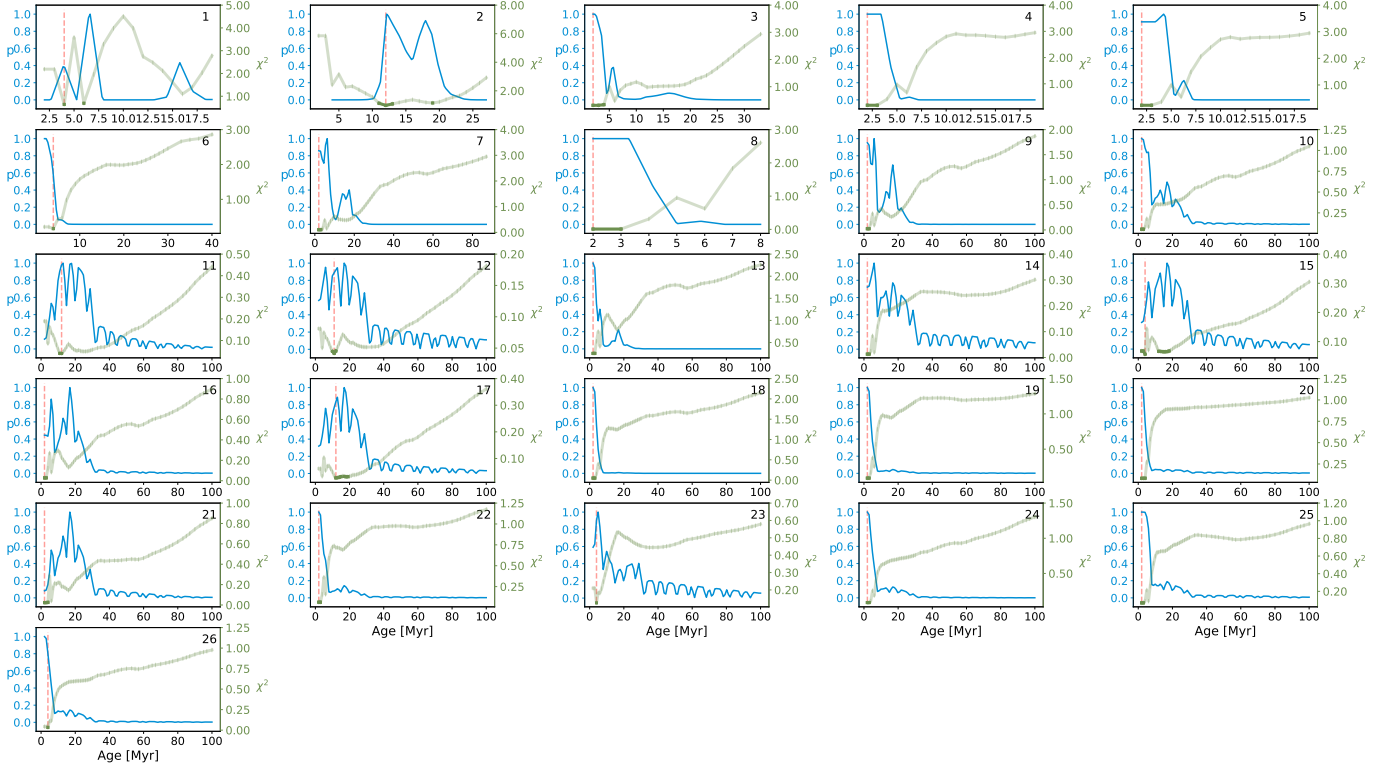


Figure B3. PDF of the age parameter for each cluster. The left y -axis shows the PDF, color-coded in blue, the right y -axis shows the corresponding χ^2 distribution, color-coded in green. The best model value, selected by Cigale and corresponding to the lowest χ^2 , is marked by a dashed red line. χ^2 values within 20% of the minimum represent models indistinguishable from the best fit, and are marked by dark green. Note that the used step size during the SED fitting can be directly inferred for each parameter from the density of points in these figures.

Schaerer, D., Contini, T., & Pindao, M. 1999, A&AS, 136, 35

Schlafly, E. F., & Finkbeiner, D. P. 2011, ApJ, 737, 103

Serra, P., Amblard, A., Temi, P., et al. 2011, ApJ, 740, 22

Smith, L. J., Crowther, P. A., Calzetti, D., & Sidoli, F. 2016, ApJ, 823, 38

Terlevich, E., Diaz, A. I., Terlevich, R., & Vargas, M. L. G. 1993, MNRAS, 260, 3

Terlevich, R., Melnick, J., Masegosa, J., Moles, M., & Copetti, M. V. F. 1991, A&AS, 91, 285

Thuan, T. X., & Martin, G. E. 1981, ApJ, 247, 823

Veilleux, S., Cecil, G., & Bland-Hawthorn, J. 2005, ARA&A, 43, 769

Zastrow, J., Oey, M. S., Veilleux, S., & McDonald, M. 2013, ApJ, 779, 76

Zastrow, J., Oey, M. S., Veilleux, S., McDonald, M., & Martin, C. L. 2011, ApJL, 741, L17

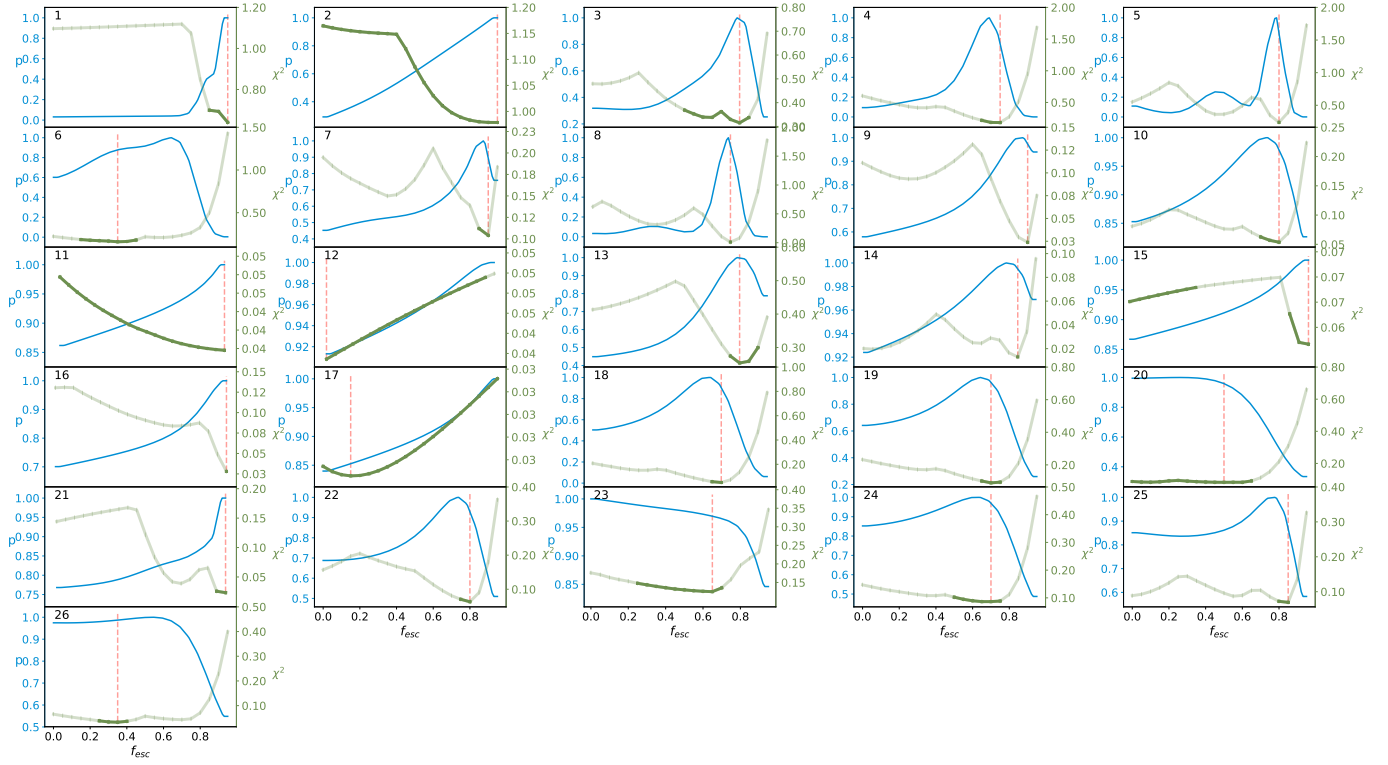


Figure B4. PDF of the f_{esc} parameter for each cluster. Line types and axes are as in Figure B3.